

6CCYB070 BEng Research Project

**Machine learning for microstructural analysis of
the fetal brain layers using multimodal MRI**



University of London

Amiruthavallii Karthi Kumar

Supervisors:

Dr. Maria Deprez

Ms. Helena Sousa

Project report submitted in partial fulfilment of the Bachelor of Engineering
in Biomedical Engineering

April 2024

ACKNOWLEDGEMENTS

I would like to express my sincere gratitude to Dr Maria Deprez for the opportunity to work on this fascinating project that combines my interests in data science and neuroscience. Her expertise in machine learning and brain imaging has been invaluable in guiding me to acquire new skills and in navigating any challenges.

I would like to extend my heartfelt thanks to Helena Sousa, whose unwavering guidance and support were integral to the successful completion of this project. Her constant advice, assistance, and patience in answering my questions were instrumental in my achieving the results described in this dissertation. Furthermore, her deep learning model played a crucial role in providing the segmentations necessary for this project.

I would also like to thank Dr Siân Wilson for providing me with background knowledge on diffusion maps and assisting with the image registration process.

Lastly, I am grateful to all the mothers and families who participated in the dHCP whose contributions made this project possible.

ABSTRACT

The past decade has seen rapid advancements in the field of diffusion-weighted imaging (DWI) and its applications in understanding fetal brain development in utero. However, the mechanisms that underpin the microstructural changes within the fetal transient layers are not fully understood. To explore this gap in understanding, this project quantitatively mapped the spatiotemporal evolution of the transient fetal compartments which included the cortical plate (CP), subplate (SP), white matter (WM), and proliferative zone (PZ) using DWI data from the Developing Human Connectome Project (dHCP). This dataset consisted of 183 fetuses, ranging from 20 to 38 weeks of gestation, 6 of whom had ventriculomegaly. A polynomial ridge regression pipeline was implemented to model the diffusion metrics extracted from the DWI data to analyse information on fractional anisotropy (FA), mean diffusivity (MD), tissue fraction (TF), and fluid fraction (FF). All regions presented non-linear trends with the exception of FA of the CP which demonstrated a linear trend in relation to gestational age. FA was found to be decreasing in all the regions and did not follow similar trends to TF. A significant finding was the synchronised peak in water content and diffusivity across all regions at similar gestational ages. No significant differences were found between healthy subjects and those with ventriculomegaly. The findings from this study are closely linked to the neurobiological processes that are happening at this stage of gestation and therefore provide valuable insight into the normal patterns of FA, MD, TF, and FF in the fetal brain.

KEYWORDS: *Fetal brain MRI, Diffusion tensor imaging, Cortical plate, Subplate, Periventricular White Matter, Proliferative Zone, Ventricular Zone, Ganglionic Eminence, Ventriculomegaly*

PROJECT PLAN

Problem

The intricacies of the microstructural changes in the rapidly developing fetal brain remain elusive due to technical challenges, such as subject motion and limited acquisition times. Most of our current understanding comes from animal brain or post-mortem studies. These limit observations of dynamic changes as different species develop differently, and post-mortem samples only provide a snapshot of the brain at a specific point.

Vast studies exist on neonatal and preterm infants however, in comparison, the fetal population remains under-researched. Pre-existing studies on the fetal population have mostly investigated brain volumetry contributing to a macroscopic view of brain development, but there remains a gap in knowledge at the microscopic level. This poses a need for a non-invasive observation method to further our understanding of fetal brain development which this study aims to address.

State of the art

Histological analysis is the gold standard for examining the microstructure of the fetal brain. However, it does not offer visualisation of the development of transient structures in utero. Furthermore, the quantity and quality of human fetal post-mortem tissue is limited (1). Ex vivo MRI provides greater resolution and there is a lack of time constraint. However, In vivo MRI allows the opportunity for real-time observations of developmental processes.

The developing Human Connectome Project (dHCP) provides high-quality structural (T2w) and diffusion (HARDI) fetal MRI data (2). A deep learning solution for automated segmentation of the transient regions has been created and tested on the dataset (3). The volumes of said transient regions have been quantified and compared between fetuses with ventriculomegaly and healthy subjects. This project will build on the segmentation method by applying machine learning to analyse the microstructural changes of those transient regions with respect to gestational age.

Aims

- Map the age-dependent transformation (microstructural changes) of the individual transient layers with each GA in normal fetal brain development by performing a regression model such as Gaussian process.
- Develop a machine learning model that is able to detect and/or predict any abnormalities or developmental delays in unseen data. Pinpoint the exact moment malformations start to occur in fetuses with ventriculomegaly.

Work plan

This project will use structural and diffusion data from 21 to 36 weeks gestational age from the final release of the dHCP (2), and existing segmentations of fetal brain transient layers (3).

Phase 1 - Develop a pipeline to align diffusion-weighted imaging (DWI) to the T2 space using FSL (4).

Phase 2 - Extract relevant features (diffusion metrics) using MRtrix3 (5). Calculate regional average values in transient compartments.

Phase 3 – Implement regression in scikit-learn combining linear and Gaussian models.

Develop a Gaussian process-based approach for accurate modelling using GPy in Python (6). Capture and model the layer-specific microstructural changes with respect to GA.

Phase 4 - Model normal individual variability and detect abnormalities and developmental delays. Comparative analysis between cohorts of subjects with normal development and those diagnosed with ventriculomegaly.

Deliverables

- Pipeline for the extraction of the markers of development.
- Growth charts as a function of age for normal fetal development (with percentiles).
- Anomaly detection technique using Gaussian-process (graph of two different cohorts).
- Develop a normative reference to supplement histological knowledge and to develop an understanding of how the microstructure is different for various conditions.

Evaluation

The success of this project will be determined by evaluating the following:

- Testing which is the best model using goodness of fit.
- Ability of the model to generalise well to unseen data.

- Ability to distinguish brain development and find and prove differences between normal and abnormal populations.

Project timeline

	Oct 23	Nov 23	Dec 23	Jan 24	Feb 24	Mar 24	Apr 24
Literature review							
Phase 1							
Phase 2							
Phase 3							
Phase 4							
Report							

NOTE

The project plan proposed the implementation of Gaussian process regression.

However, polynomial ridge regression was chosen to be implemented instead. This decision was made after a thorough examination of the extracted data, which indicated that polynomial ridge regression serves as a suitable introductory model. Additionally, the regularisation capabilities of ridge regression were deemed advantageous for handling the noisy nature of the dataset used in this project. The results confirmed the efficacy of this alternative approach. Nevertheless, it should be noted that Gaussian process remains a viable option for future exploration due to its inherent capability to provide probabilistic predictions which may offer valuable insights into uncertainty estimations.

Table of Contents

1	INTRODUCTION AND BACKGROUND	15
1.1	The fetal brain development.....	15
1.2	Transient regions in the fetal brain	16
1.2.1	Cortical plate	19
1.2.2	Subplate.....	19
1.2.3	White matter/ intermediate zone	20
1.2.4	Proliferative zone.....	20
1.3	Structural and diffusion MRI imaging	22
1.3.1	Diffusion-weighted imaging.....	22
1.3.2	Diffusion tensor imaging	23
1.3.3	Constrained spherical deconvolution	26
1.4	Challenges of in utero dMRI	28
1.5	State of the art	29
1.5.1	Automatic segmentation of the fetal brain.....	29
1.5.2	Microstructural analysis of the fetal brain.....	31
1.5.3	Aims and objectives	32
2	MACHINE LEARNING THEORY	33
2.1	Polynomial ridge regression	33
2.1.1	Model evaluation.....	34

3	METHODS	35
3.1	Subject data	35
3.1.1	The developing Human Connectome Project.....	35
3.1.2	Diversity of data	36
3.2	Data acquisition.....	36
3.3	Diffusion modelling	37
3.4	Data pre-processing.....	38
3.4.1	Segmentation	38
3.4.2	Feature extraction	40
3.5	Polynomial ridge regression and model evaluation.....	40
3.6	Analysis of VM subjects	42
4	RESULTS	44
4.1	Polynomial ridge regression model	45
4.2	Model evaluation.....	51
4.3	Analysis of VM subjects	52
5	DISCUSSION	54
5.1	Analysis of results	54
5.2	Comparison to the state of art.....	56
5.3	Limitations	58
6	CONCLUSION	59

6.1	Future work	59
7	REFERENCES	61
8	APPENDIX	66

List of Figures

Figure 1: 3D reconstructions of the fetal brain development through gestational age showing formations of gyri (bumps) and sulci (grooves). PCW – post-conception weeks. Taken from (10).	16
Figure 2: The fetal brain layers at gestational ages 21, 28, and 36 represented by T2w brain MRI atlas. Adapted from (11).....	17
Figure 3: Timeline of various neurobiological developmental processes occurring from conception to birth. Processes within the second and third trimester are highlighted and marked as the period which is visible in utero fetal MRI. Image supplied by Dr. Sian Wilson.....	18
Figure 4: Example of VM in fetal brain MRI (26 weeks of GA). The ventricle highlighted by the red arrow shows abnormal enlargement compared to the ventricle in the opposite hemisphere.	21
Figure 5: Representations of fibre configurations and corresponding tensor ellipsoid and diffusion signal. Left and centre fibre configurations show straight coherent fibre bundles which are well described by the tensor model. The fibre configuration on the right shows 'crossing fibres' that the tensor model struggles to represent using an ellipsoid. Taken from (21).	24
Figure 6: Anisotropic diffusion represented as an ellipsoid showing three unit eigenvectors and corresponding eigenvalues. Taken from (25).....	25
Figure 7: Estimated fODFs from DWI images using MSMT-CSD showing WM, GM, and CSF. Taken from (29).....	27

Figure 8: Segmentation of the fetal brain in 19 labels (left and right) using automated multi-label segmentation tool from BOUNTI showing maps of 21, 26, 31 and 36 weeks GA of the dHCP fetal brain DWI atlas. Taken from (34).	30
Figure 9: 3D segmentations and volumetric analysis of transient regions - SP, VZ and GE at varying GAs by (3).	30
Figure 10: Trends of median FA and MD across GA for whole brain, CP, SP, IZ and GE from Calixto et al. Taken from (35).	31
Figure 11: Trends of mean FA, MD, TF and FF across GA for CP and SP from Wilson et al. Taken from (36).	32
Figure 12: Histogram of fetal MRI dataset from dHCP showing the distribution of GAs.	35
Figure 13: T2w image of a 30-week fetus along with the corresponding FA, MD, TF, and FF.....	37
Figure 14: Axial, coronal, and sagittal views of five fetal subjects of 21, 24, 28, 33, and 36 GAs with the CP, SP, PZ, PVWM, and WM segmentation labels overlayed on their T2w images.	39
Figure 15: Summarised pipeline of methodology.	43
Figure 16: Four polynomial ridge models showing FA, MD, TF, and FF of the whole brain vs GA along with the polynomial degree and L2 penalty chosen by the cross-validation. The train set R^2 score of each model is also shown on the plots. VM subjects are highlighted in red.	46
Figure 17: Four polynomial ridge models showing FA, MD, TF, and FF of the CP vs GA along with the polynomial degree and L2 penalty chosen by the cross-validation. The train set R^2 score of each model is also shown on the plots. VM subjects are highlighted in red.....	47

Figure 18: Four polynomial ridge models showing FA, MD, TF, and FF of the SP vs GA along with the polynomial degree and L2 penalty chosen by the cross-validation. The train set R^2 score of each model is also shown on the plots. VM subjects are highlighted in red.....	48
Figure 19: Four polynomial ridge models showing FA, MD, TF, and FF of the WM vs GA along with the polynomial degree and L2 penalty chosen by the cross-validation. The train set R^2 score of each model is also shown on the plots. VM subjects are highlighted in red.....	49
Figure 20: Three polynomial ridge models showing MD, TF, and FF of the PZ vs GA along with the polynomial degree and L2 penalty chosen by the cross-validation. Scatter plot of FA shown as no suitable model was found. The train set R^2 score of each model is also shown on the plots. VM subjects are highlighted in red.	50
Figure 21: Polynomial ridge model of FA of the GE vs GA along with the polynomial degree and L2 penalty chosen by the cross-validation. The train set R^2 score of the model is also shown on the plot. VM subjects are highlighted in red.....	50
Figure 22: Box plots of CP - MD, FF, and SP - FA, FF comparing the z-scores of healthy and VM subjects.	52
Figure 23: Comparison of FA and MD of WM/ IZ between results from Calixto et al. and results from this project. Top two plots taken from (35).	57

List of Tables

Table 1: Definitions of the major neurogenic events that occur in the fetal transient layers across gestation adapted from (12).....	17
Table 2: Hyperparameters used in cross validation.	41
Table 3: Summary of observed trends in FA, MD, TF, and FF across all ROIs. In regions where a change of trajectory was observed, the GA at the inflection point (IP) has been identified.....	45
Table 4: Comparison of R^2 scores of train and test sets for all models. Train set scores are shaded in grey with test set scores below them.	51

1 INTRODUCTION AND BACKGROUND

1.1 The fetal brain development

The human brain development begins in the third week of gestation and extends to almost three decades. Many individuals might consider the most intriguing aspect of brain development to be the transition from a small, smooth structure to one with intricate folding. However, besides the mechanical changes such as that, numerous microstructural changes enable the incredible functionality of the human brain allowing it to orchestrate complex processes such as consciousness, language, and reasoning.

In utero, various processes including neuron production, migration and differentiation take place. In terms of the microstructure, it begins when neural progenitor cells (stem cells that can only differentiate into specific cell types) begin to divide and differentiate into two cell types that form the basis of the nervous system: neurons and glia (7).

Neurons are capable of electrical and chemical conductivity and transmission whereas glia maintain the microenvironment for these neurons by regulating ion concentration and repairing damage (8). In addition, the crucial pathways that allow the transmission of sensory and motor information between the thalamus and the cerebral cortex, such as the thalamocortical and corticothalamic pathways, also occur. Newly produced neurons migrate to various regions of the brain to initiate connections with other neurons constructing core neural networks (7).

Any alterations in these processes can lead to neurodevelopmental disorders which can severely affect the quality of life of individuals and their families. The prevalence of neurodevelopmental disorders arising from impaired brain development in utero is estimated at 1 in 30 live births (9).

The causal factors and neurobiological basis of these conditions are not fully understood. Therefore, establishing a normative reference for fetal brain development will provide a clearer picture of the biological pathways and help identify deviations that occur in cases such as autism, down syndrome, ventriculomegaly and congenital heart disease. This is crucial in aiding early diagnosis and management by allowing healthcare providers and parents to plan perinatal and postnatal care more effectively, thus improving patient outcomes.

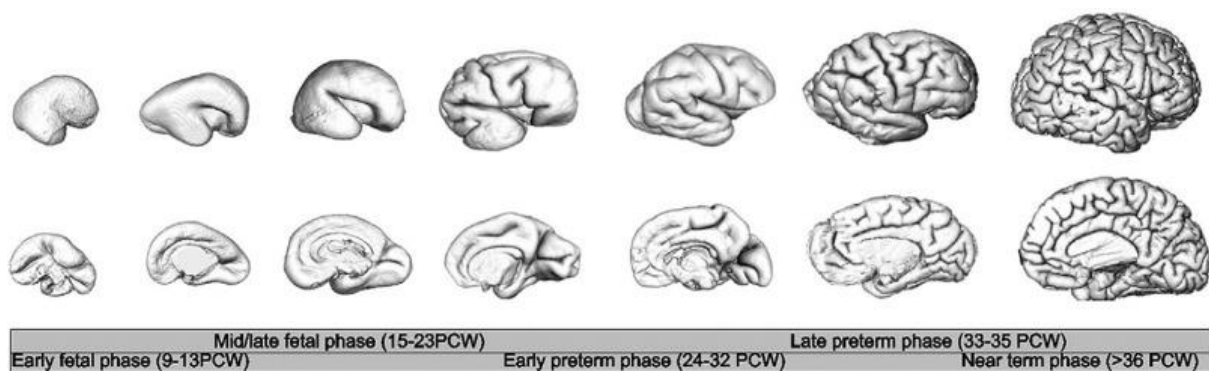


Figure 1: 3D reconstructions of the fetal brain development through gestational age showing formations of gyri (bumps) and sulci (grooves). PCW – post-conception weeks. Taken from (10).

1.2 Transient regions in the fetal brain

The cytoarchitecture and role of the transient regions of the fetal brain remain unclear despite the advancements in imaging techniques. The project focuses heavily on uncovering the microstructural changes in fetal transient regions during the end of the second trimester and the beginning of the third (20-38 weeks of gestational age). Therefore, it is imperative to have a basic understanding of the maturation happening in these structures at this time.

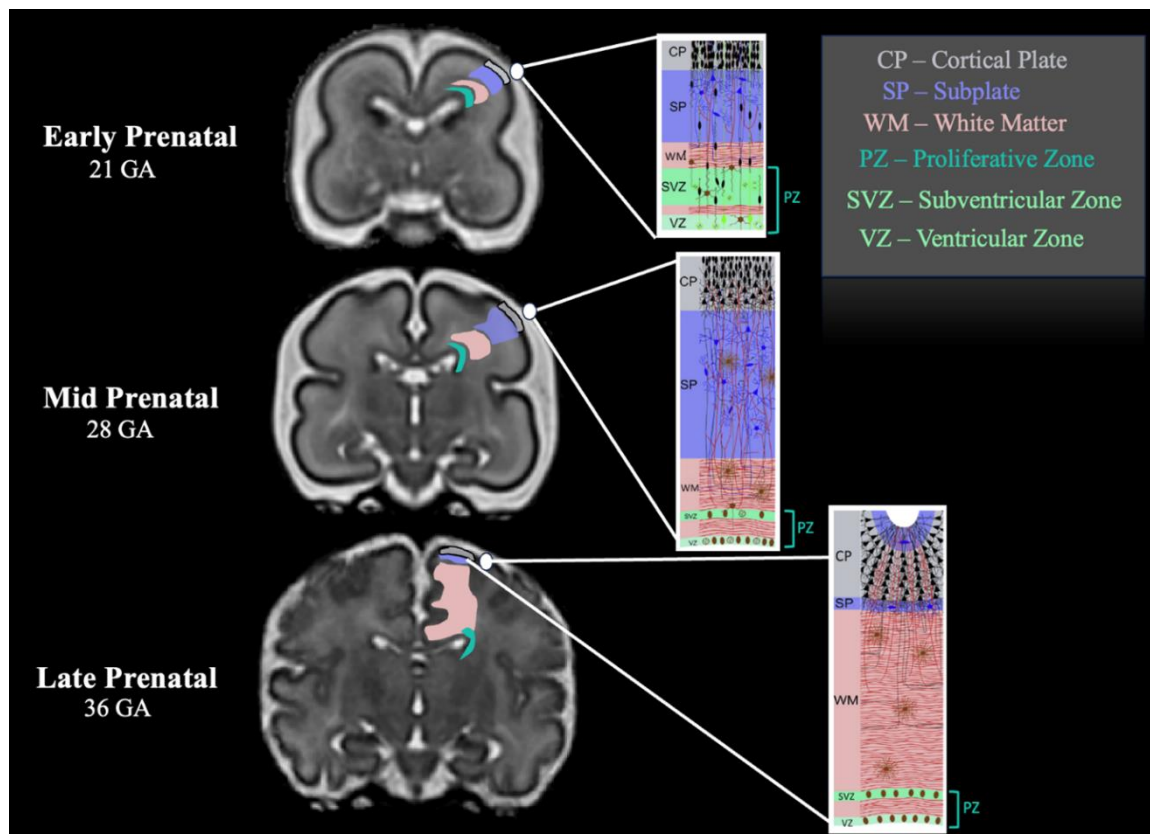


Figure 2: The fetal brain layers at gestational ages 21, 28, and 36 represented by T2w brain MRI atlas. Adapted from (11).

Cell proliferation	The increase in the number of cells resulting from cell division.
Neurogenesis	The generation of new neurons.
Gliogenesis	The generation of new glial cells (non-neuronal cells).
Neuronal migration	The process where neurons move from their regions of origin in the VZ and SVZ to their appropriate destinations in the brain.
Neuronal aggregation	The clustering of specialised nerve cells to form functional structures.
Axonal outgrowth	Nerve cells extend long, threadlike projections which carry nerve impulses from the cell's body.
Dendritic arborisation	The tree-like branching process of dendrites (input points of neurons)
Synaptogenesis	The formation of synapses which is the gap between neurons where nerve impulses are transmitted.
Myelination	The formation of myelin sheath around neurons which facilitates efficient conduction of electrical impulses.

Table 1: Definitions of the major neurogenic events that occur in the fetal transient layers across gestation adapted from (12).

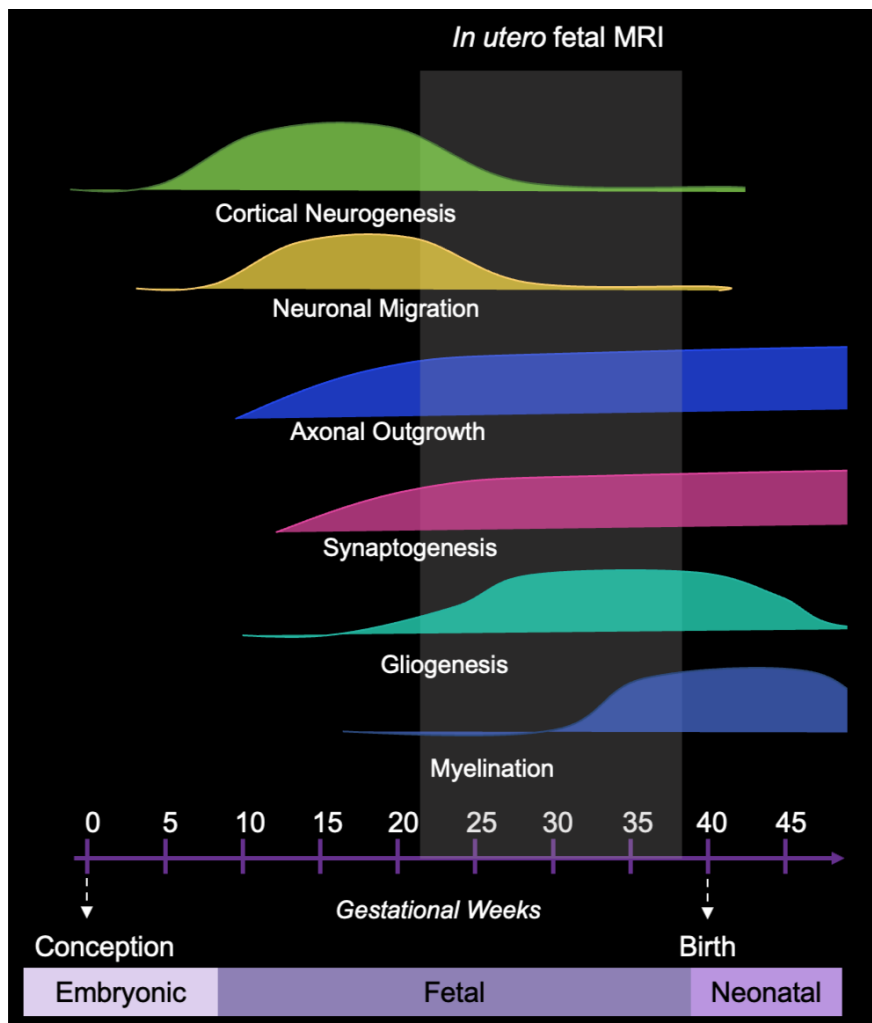


Figure 3: Timeline of various neurobiological developmental processes occurring from conception to birth. Processes within the second and third trimester are highlighted and marked as the period which is visible in utero fetal MRI. Image supplied by Dr. Sian Wilson.

Transient layers in the fetal brain include the cortical plate (CP), subplate (SP), white matter known as the intermediate zone (IZ) and proliferative zone (PZ) which comprises the subventricular zone (SVZ) and ventricular zone (VZ) (10). These regions undergo temporary structural and functional changes and are defined on structural fetal MRI by heterogeneous and stratified signal intensities. They exhibit rapidly changing patterns throughout the gestational ages which this report aims to explore.

1.2.1 Cortical plate

The cortical plate (CP) is a key structure in the development of the cerebral cortex which is responsible for most of the 'human' experiences such as thinking, remembering, and feeling emotions along with sensory and motor functions. The CP undergoes significant changes during gestation. At 20 weeks of gestational age (GA), the CP reaches its peak in neuronal migration and is densely filled with post-migratory cells. Between 21-28 weeks of GA, this compartment grows exponentially due to processes such as synaptogenesis, dendritic arborisation and axonal growth, leading to the appearance of cortical folding (13). These processes disrupt the predominantly radial organisation of the cortical plate during this period until term age. Throughout gestation, the CP appears as a dark region (low-intensity signal) in T2-weighted (T2w) in utero MRI due to its high cell density.

1.2.2 Subplate

The SP develops underneath the CP and acts as a waiting compartment for various tasks such as neuronal differentiation and migration. It acts as a hub for synaptogenesis facilitating the establishment of crucial connections in various parts of the brain such as the thalamus (processes sensory information) and cortex (involved in thinking) (10). In T2w in utero MRI, the SP appears as a bright region due to its water-rich content and low tissue density. It is particularly prominent during mid gestation around 26 weeks of GA where it is at its thickest and becomes the most differentiated zone containing post-migratory neurons. After this period, around 30 weeks of GA, the extracellular matrix in the SP starts to reduce as the thalamocortical fibres start to migrate to the CP.

Therefore, the SP starts to progressively diminish and becomes less visible in the later stages of development (10).

1.2.3 White matter/ intermediate zone

The IZ is the region containing fetal white matter (WM). It is situated between the cortical plate and the proliferative zone as seen in Figure 2. This region is the site of axonal growth, migratory neurons and immature glial cells (14).

Periventricular white matter

A subpart of WM/IZ is periventricular white matter (PVWM). This region is a hotspot for white matter maturation in the developing brain reflecting processes such as radial glial scaffolding disassembly and cortical plate lamination. Radial glial cells are cells that play a critical role in the development of the brain and the spinal cord as they form a scaffold of long fibres to guide the migration of neurons to their appropriate destinations (15).

1.2.4 Proliferative zone

The regions described below containing tightly packed proliferative cells are referred to as the proliferative zone. They surround the ventricles of the fetal brain as seen in Figure 2. It is known that neuronal cells migrate from the proliferate zones to the CP and proliferate there (11), with cell migration and proliferation occurring heavily in the second trimester and gradually ceasing during the third trimester. Insufficient cell proliferation and migration in the PZ is linked to neurodevelopmental abnormalities, such as ventriculomegaly (VM), which is a condition characterised by abnormal enlargement of the ventricles in the brain (16).

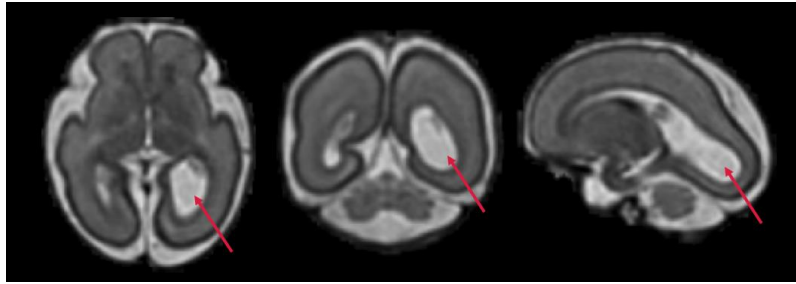


Figure 4: Example of VM in fetal brain MRI (26 weeks of GA). The ventricle highlighted by the red arrow shows abnormal enlargement compared to the ventricle in the opposite hemisphere.

Ventricular zone

The VZ is a specific layer of tissue in the PZ containing densely packed proliferative cells. This region is responsible for the production of neurons which will later migrate and constitute the subplate and the cortical plate (10). VZ reaches its peak in thickness at around 23 weeks of GA, followed by a decrease in thickness after around 30 weeks of GA which is visible in fetal MRI (11).

Ganglionic eminence

The ganglionic eminence (GE) corresponds to the thick and bulbous part of the PZ (10) and produces progenitor cells which are partially differentiated stem cells that can fully differentiate to form different types of specialised cells. It appears as the darkest region (lower intensity values) of the PZ in T2w MRI (11).

With the precise developmental trajectory of these transient regions in-utero still being poorly understood, multimodal MRI surges as a strong candidate to explore both structural and microstructural neurodevelopment of the fetal brain. This exploration poses an opportunity to gain insights into the precise timings of biological processes of cell migration and proliferation as well as to identify features of abnormal neurodevelopment.

1.3 Structural and diffusion MRI imaging

In comparison to other commonly used imaging techniques such as ultrasound (US), magnetic resonance imaging (MRI) offers a much higher resolution allowing for the detailed analysis of rapidly developing regions.

In clinical practice, the T2-weighted (T2w) MRI sequence is usually used for highlighting anatomical details in the fetal brain. In particular, the T2w Single-Shot Fast Spin Echo (SSFSE) sequence (17) is widely used to acquire fetal data in utero. It enables quick acquisition of images, making it especially suitable for imaging the fetal brain. However, fetal MRI acquisition is often still challenging due to severe fetal motion in the uterus, which frequently results in noisy images with motion artefacts. Challenges in fetal MRI will be further discussed in section 1.4.

1.3.1 Diffusion-weighted imaging

In addition to the structural information gathered from T2w, diffusion-weighted imaging (DWI) is a complementary neuroimaging tool for obtaining information about the microstructure of biological tissues. DWI measures the motion of water diffusion across tissues, offering comprehensive information on intracellular and extracellular water diffusion. Therefore, it provides valuable information about the structural integrity and connectivity of brain tissues, as well as the normative patterns of brain development that go beyond what can be conveyed solely through structural MRI.

When water diffuses equally in all directions, the diffusion is called isotropic. Whereas, when the diffusion is not equal all in 3-dimensional directions, it is considered to be anisotropic. In the brain, areas with cerebrospinal fluid will demonstrate isotropic

diffusion but anisotropic diffusion takes place in white matter. This is because water molecules diffuse more easily along the length of axons (longitudinal axis) than across them (18). This diffusion is also influenced by the presence of obstacles such as cell membranes, fibres, and macromolecules.

The protons in water molecules are responsible for generating the signal in DWI where areas of free movement exhibit low signal such as the ventricles and areas where movement is restricted have higher signal (19).

Modelling the diffusion signal enables us to correlate and corroborate with known histological knowledge to comprehend the underlying biological mechanics in a data-driven manner. Furthermore, histological techniques can only offer a singular glimpse of the brain tissue at a particular instant in time, lacking the capability to analyse the spatiotemporal progression, especially in water-rich regions such as the SP. Given the rapid pace of fetal brain development, diffusion MRI (dMRI) facilitates a more comprehensive mapping of the maturation processes.

1.3.2 Diffusion tensor imaging

Diffusion tensor imaging (DTI) is a widely used type of dMRI which enables the description of the local water molecules using a Gaussian model (20). It is a modelling technique that enables the creation of a mathematical model (diffusion tensor), which reflects the dominant direction of water diffusion.

However, there are several limitations to diffusion tensor imaging. The primary concern is that the crossing of fibre tracts in the human brain cannot be well described by the diffusion tensor (20). ‘Crossing fibres’ refers to any situation where the fibre orientation

is not clear, these include scenarios such as intertwining fibres, or when fibres bend or diverge creating uncertainty in their orientation (21).

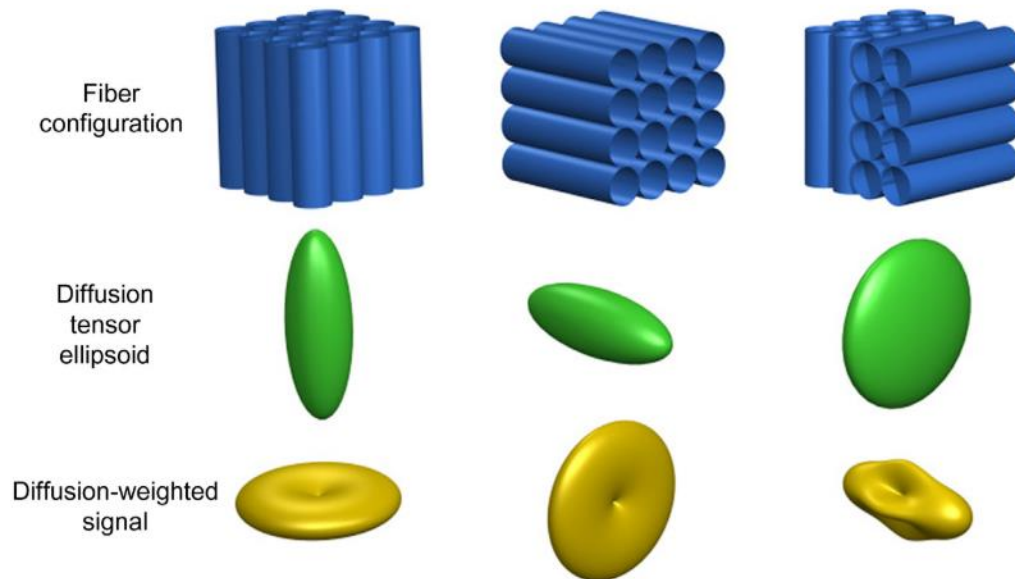


Figure 5: Representations of fibre configurations and corresponding tensor ellipsoid and diffusion signal. Left and centre fibre configurations show straight coherent fibre bundles which are well described by the tensor model. The fibre configuration on the right shows 'crossing fibres' that the tensor model struggles to represent using an ellipsoid. Taken from (21).

High angular resolution multi-shell diffusion-weighted imaging

An extension of DTI is a higher-order acquisition protocol known as high angular resolution multi-shell diffusion-weighted imaging (HARDI) which can capture more complex fibre orientations. This is accomplished by measuring the DWI signal using a higher number of uniformly distributed gradient directions than necessary for DTI to capture the higher angular frequency aspects of the DWI signal that are not sufficiently modelled by a single diffusion tensor (22).

From HARDI data, quantitative diffusion metrics such as fractional anisotropy (FA) and mean diffusivity (MD) are derived.

Fractional anisotropy

FA is a scalar derivative of diffusion-tensor imaging which provides insight into the directionality of water diffusion (23). FA values range between 0 (infinite isotropy) indicating unrestricted water movement in all directions of the brain and 1 (infinite anisotropy) indicating a highly directional movement of water (24).

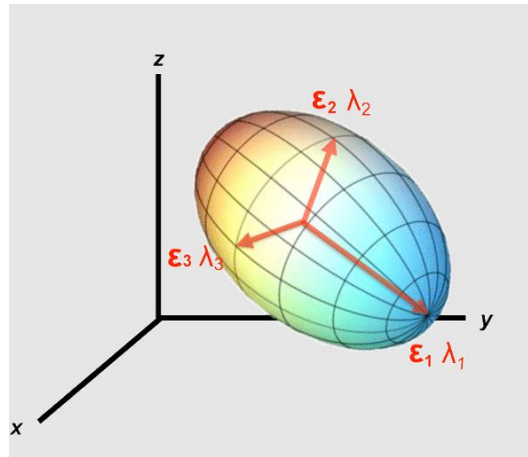


Figure 6: Anisotropic diffusion represented as an ellipsoid showing three unit eigenvectors and corresponding eigenvalues. Taken from (25).

$$FA = \sqrt{\frac{1}{2} \frac{\sqrt{(\lambda_1 - \lambda_2)^2 + (\lambda_2 - \lambda_3)^2 + (\lambda_3 - \lambda_1)^2}}{\sqrt{\lambda_1^2 + \lambda_2^2 + \lambda_3^2}}} \quad (1)$$

Equation 1: Derivation of FA in terms of the diffusion tensor eigenvalues.

Mean diffusivity

The average of the eigenvalues $(\lambda_1 + \lambda_2 + \lambda_3)$ is referred to as MD (26). MD in diffusion imaging quantifies the average rate of water diffusion in tissue. Lower MD reflects higher tissue density and vice versa. When structurally organised tissue such as white matter tracts degenerate, it correlates with an increase in MD but a decrease in FA as there is a loss in directionality (27).

$$MD = \frac{\lambda_1 + \lambda_2 + \lambda_3}{3} \quad (2)$$

Equation 2: Derivation of MD in terms of the diffusion tensor eigenvalues.

In summary, FA is the degree to which diffusion is confined to one direction and MD measures the overall diffusion that occurs in a 3D voxel.

However, between one-third to two-thirds of white matter are believed to be areas of fibre bundle crossings where, as mentioned earlier, the diffusion tensor model is not complete. Therefore, this may provide misleading information regarding the underlying tissue microstructure in these regions (28).

1.3.3 Constrained spherical deconvolution

Constrained spherical deconvolution (CSD) is introduced as an attempt to overcome the limitations of DTI in areas with crossing fibres. This method estimates the complete fibre orientation distribution function (fODF) in each voxel. However, CSD can only produce noise-free fODF estimates in voxels containing only white matter (WM) and becomes unreliable when met with other tissue types such as grey matter (GM) and cerebrospinal fluid (CSF) (29).

Therefore, an adaptation of CSD which supports multi-shell data known as multi-shell multi-tissue constrained spherical deconvolution (MSMT-CSD) is applied to the HARDI data. This technique relies on the assumption that DWI signal comes from three types of tissues in the brain: WM, GM, and CSF. It also assumes that the response function from WM is isotropic and the response functions from GM and CSF are anisotropic. In doing so, MSMT-CSD divides the diffusion signal into distinct tissue types (30) and has been shown to produce reliable volume fraction maps of WM, GM and CSF directly from DWI data (29).

This method gives rise to two more diffusion metrics known as tissue fraction (TF) and fluid fraction (FF).

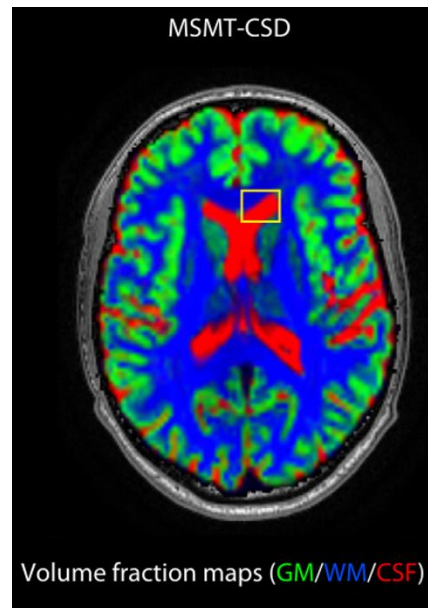


Figure 7: Estimated fODFs from DWI images using MSMT-CSD showing WM, GM, and CSF. Taken from (29).

Tissue fraction

TF represents the signal from the actual 'white matter like' tissue in each voxel.

Fluid fraction

Fluid fraction constitutes fluid or cerebrospinal fluid (CSF). CSF exhibits a distinct diffusion signal due to its high water content. This makes it easily distinguishable from WM and GM (29).

MD and FF are analogous as they both assess water content - a higher water fraction results in increased diffusivity. TF and FA are complementary in nature as they both examine tissue characteristics, but with a distinction - FA examines tissue directionality while TF evaluates the quantity of tissue present in a specific region. High TF would indicate a high volume of tissue. However, if the fibres are not aligned, the averaging

effect would cause the overall diffusion signal to become less directional (more isotropic) therefore leading to a lower FA in areas of crossing fibres. High FF, however, would suggest high MD as there would be more unrestricted diffusion in regions with higher water content.

1.4 Challenges of in utero dMRI

There are several challenges in acquiring fetal DWI data including safety constraints and subject motion which affect the resolution of the images and can introduce unwanted noise in the data.

The fluid-filled environment within the uterus reduces the rate of heat loss. Therefore, it is crucial to prevent tissue heating. This limits the use of strong gradients which impacts image quality. Additionally, longer scan times may cause maternal discomfort meaning the scan time may also be limited (31).

dMRI is affected by both maternal breathing as well as the rapid, unpredictable movements of the fetus as this can induce abrupt signal dropout (31). Additionally, since MRI scanning typically requires more time than other imaging modalities, there is an increased risk of motion artefacts.

Imaging the fetal brain in particular has an added layer of complexity as the maternal abdominal tissues limit the minimum distance feasible between the MRI coil and the region of interest (31). This can lead to signal attenuation, image distortion and limited spatial resolution.

These constraints demand post-acquisition processing techniques to recover high-quality dMRI images. The techniques employed on the dataset utilised in this project are outlined in section 3.2.

Additionally, the motion artefacts are sometimes severe and result in low image resolution and contrast. This makes segmentations of the fetal brain in MRI (especially transient layers) a challenging task when coupled with the dynamic nature of fetal brain development. Moreover, manual segmentation of the MRI images is an extremely time-consuming process that requires experts on fetal brain anatomy.

1.5 State of the art

1.5.1 Automatic segmentation of the fetal brain

As mentioned in section 1.4, manual segmentation of MRI images tends to be time-consuming and is subject to observer variability.

Results presented in (32) showed how different machine learning models can accurately perform multi-label segmentation in 3D T2w fetal brain MRI by using models based on convolutional neural networks. These methods accurately segmented 7 main tissues of the brain in individual subjects with GAs ranging from 20 to 35 weeks.

However, these and other publicly available machine learning solutions for segmenting the individual fetal brain in MRI, usually only delineate the WM as a single tissue component (33), therefore not including the transient layers of the fetal brain.

Similarly, work by Uus et al. (34) has also demonstrated the feasibility of using a 3D neural network for segmenting 19 high-resolution labels of the fetal brain regions from

21-38 weeks of GA in individual subjects as shown in Figure 8. However, this also lacked labels of transient regions such as SP, VZ, GE and PVWM.

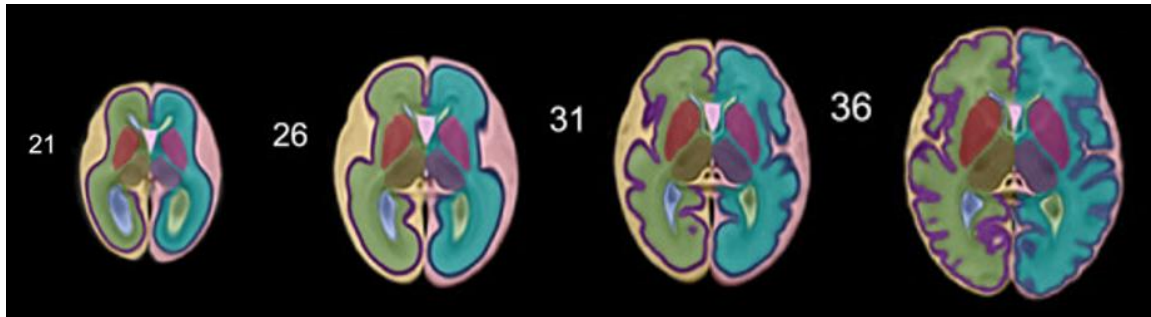


Figure 8: Segmentation of the fetal brain in 19 labels (left and right) using automated multi-label segmentation tool from BOUNTI showing maps of 21, 26, 31 and 36 weeks GA of the dHCP fetal brain DWI atlas. Taken from (34).

More recent work from Sousa et al. (3), proposed an extension of this work to automatically segment 25 regions of the fetal brain in T2w MRI, now including the left and right segmentations of transient fetal regions (SP, VZ and GE). Moreover, this work described the normal volumetric evolution of the fetal brain compartments from 21-36 weeks of GA, using 265 healthy and 8 VM subjects from the dHCP dataset (2), although missing a microstructural point-of-view.

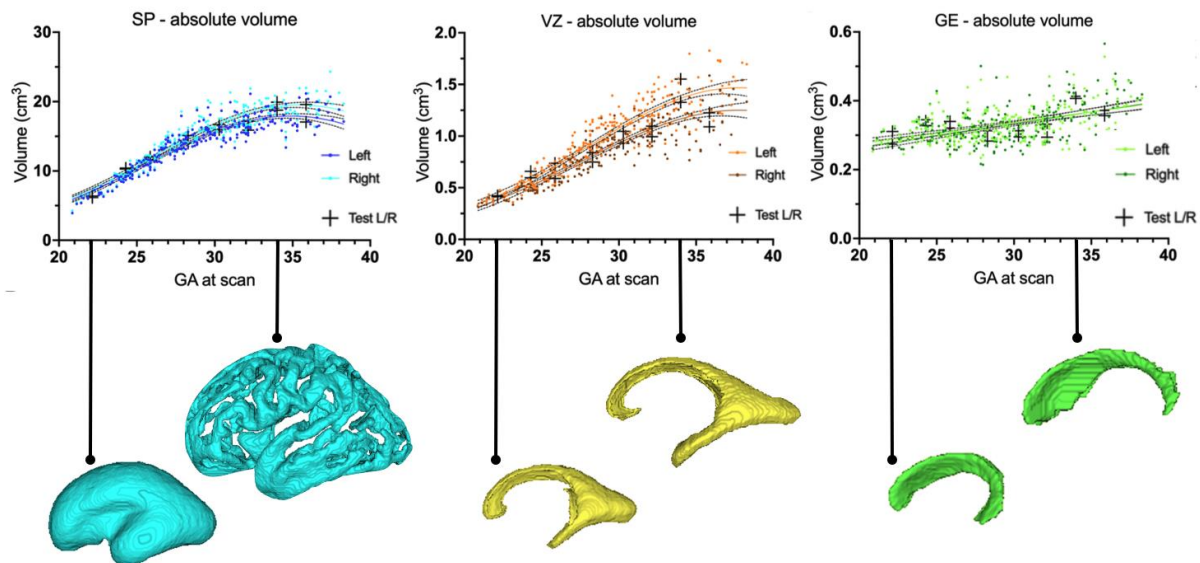


Figure 9: 3D segmentations and volumetric analysis of transient regions - SP, VZ and GE at varying GAs by (3).

1.5.2 Microstructural analysis of the fetal brain

Over the last few years, advancements in fast imaging and post-processing methods have made the use of dMRI more feasible to study. However, more extensive studies have been done on the neonatal brain, leaving the fetal microstructure poorly explored. The two studies that have conducted research most closely related to this project will be discussed next.

Calixto et al. (35) utilised DTI images from 44 fetuses to study the microstructural changes in the healthy fetal brain between 23 and 36 weeks of gestation. Statistical analysis on FA and MD was done on 14 regions of interest (ROIs) including the cortical plate, subplate, periventricular white matter, intermediate zone, and ganglionic eminence. A combination of both linear and nonlinear models were fitted and the points of change in trajectory for nonlinear trends were identified.

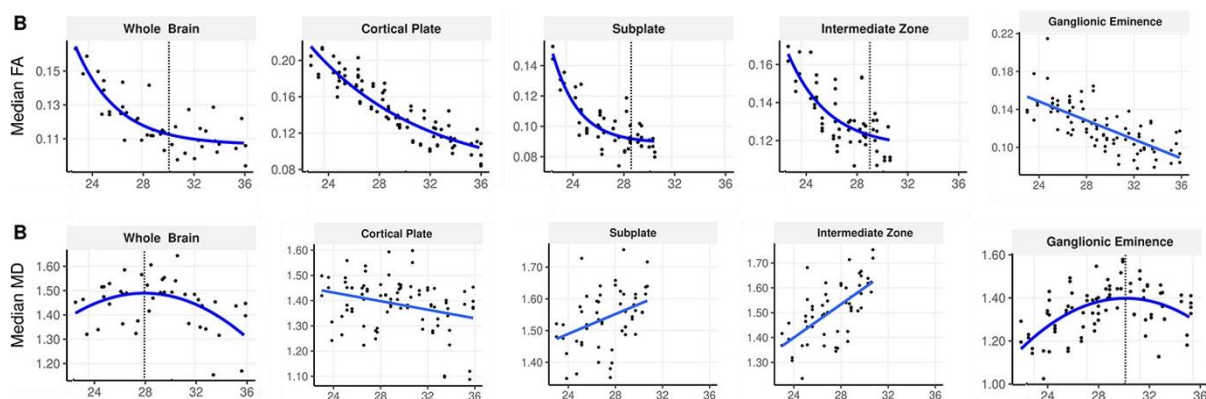


Figure 10: Trends of median FA and MD across GA for whole brain, CP, SP, IZ and GE from Calixto et al. Taken from (35).

Secondly, Wilson et al. (36) quantified the microstructural changes in SP and CP at the initial stages of cortical folding in the fetal brain, using HARDI and T2w MRI of dHCP subjects, ranging from 24 to 36 weeks of GA. They propose the modelling of the diffusion signal using DTI and MSMT-CSD to analyse different components of the

diffusion signal. The metrics derived from these models (FA, MD, TF, and FF) were used to quantify the microstructure of the SP and CP, highlighting the variation of diffusion patterns across GAs. Results showed mean MD and FF decreasing with GA in the SP and CP, while mean FA decreased linearly and TF was stable up to 30 GA followed by a rapid increase in the later GAs.

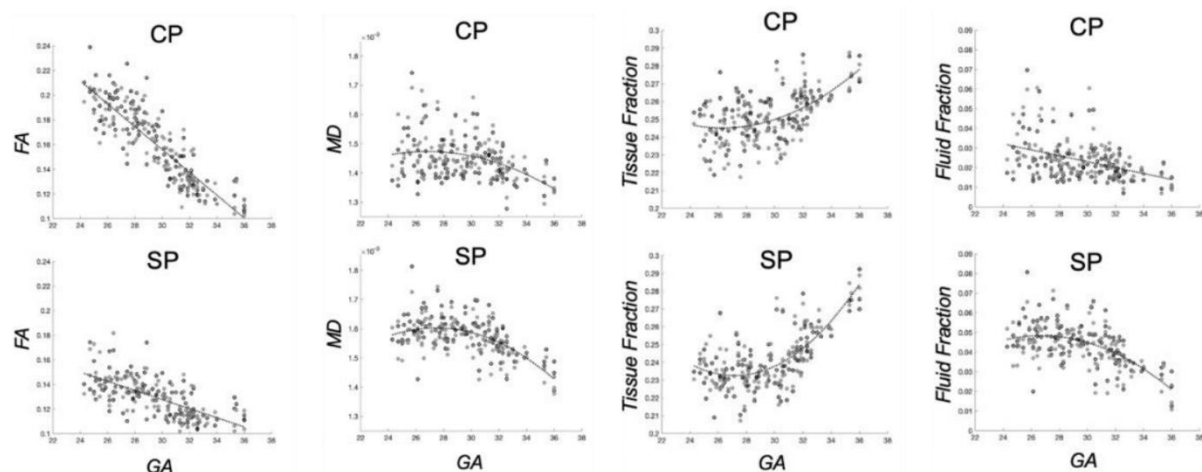


Figure 11: Trends of mean FA, MD, TF and FF across GA for CP and SP from Wilson et al. Taken from (36).

In summary, these studies provided preliminary insight into the normative trends of DTI and MSMT-CSD derived metrics in transient regions of the fetal brain. To further our understanding of the patterns in both typical and atypical fetal brain development, it is essential to further explore FA, MD, TF, and FF across a wider range of GAs in fetuses with both normal and abnormal brain development.

1.5.3 Aims and objectives

This project seeks to address the gap in knowledge surrounding the microstructure of the fetal brain layers by examining the spatiotemporal evolution of the microstructure of the transient layers from 20 to 38 weeks of GA. The fundamental aim of this project is to discover trends in the fetal transient regions across this period of neurodevelopment and establish correlations with the underlying neurobiological processes occurring in

the brain. An alteration in the neurodevelopmental process can lead to life-changing outcomes in brain function so it is essential to analyse how the trends may vary in abnormal brain development. The specific objectives are:

- To extract diffusion metrics from DWI data for the ROIs which include CP, SP, WM, PZ and additionally the whole brain, PVWM and GE.
- To implement suitable regression models to map the extracted metrics across GA in order to find correlations with histological knowledge and evaluate the models on unseen data.
- To detect any anomalies in subjects with VM.

2 MACHINE LEARNING THEORY

2.1 Polynomial ridge regression

This project employed a type of supervised machine learning method known as polynomial ridge regression. This is an implementation of penalised non-linear regression models which makes use of a combination of non-linear feature transformation, regularisation, and linear regression model fitting.

The ‘polynomial’ in the model’s name relates to the step where the input feature X , is transformed into polynomial features (X^2 , X^3 , etc.). The polynomial degree is a hyperparameter to be optimised depending on the level of the non-linear relationship between the input feature and the target variable.

However, higher degree polynomials can cause the model to become overly complex and lead to overfitting. This is where the ‘ridge’ part comes in.

Ridge regression aims to find a weight vector that minimises the loss function by incorporating a penalty to the loss function to discourage weights with very large magnitudes. The penalty term is defined as the squared L2 norm of the weight vector, which is equal to the sum of squares of individual weights. The penalty term is controlled by the hyperparameter λ , which determines the strength of the penalty term and, consequently, the extent of regularisation applied (37).

$$\tilde{E}(w) = \frac{1}{2} \sum_{n=1}^N \{y(x_n, w) - t_n\}^2 + \frac{\lambda}{2} \|w\|^2 \quad (3)$$

Equation 3: Cost function for ridge regression. $\tilde{E}(w)$ represents the value of the cost function to be minimised. y represents the predicted value of the target variable for the i -th data point, based on the current weight vector, w . t represents the n -th actual value of the target variable. w is the weight vector containing the coefficients of the model. λ is the L2 penalty imposed on the weight vector magnitude (37).

When L2 penalty (λ) is set to 0, the equation takes the form of a typical non-penalised regression, while high values of λ prevent the model from overfitting to the data and effectively penalise overly complex models.

Choosing the optimal polynomial degree and L2 penalty is essential to building a model that fits the data without overfitting. A robust method for this selection process is to use cross validation in the hyperparameter tuning step followed by validation on new, unseen data.

2.1.1 Model evaluation

R^2 score (ranges between 0 and 1) is used as an evaluation metric for regression models. It measures the proportion of variance in the target variable that can be explained by the features. It acts as the goodness of fit of a model to the dataset indicating how well the regression model can capture the variability in the target variable. R^2 score of 1 denotes a perfect fit (38).

3 METHODS

3.1 Subject data

3.1.1 The developing Human Connectome Project

The T2w and HARDI data used in this project were acquired as part of the open-source developing Human Connectome Project (dHCP) (2). The dataset produced by the dHCP contains a large number of multimodal fetal MRI. This is allowing the scientific community to study normal and abnormal fetal brain development by giving access to both structural and diffusion data of the developing human brain (2).

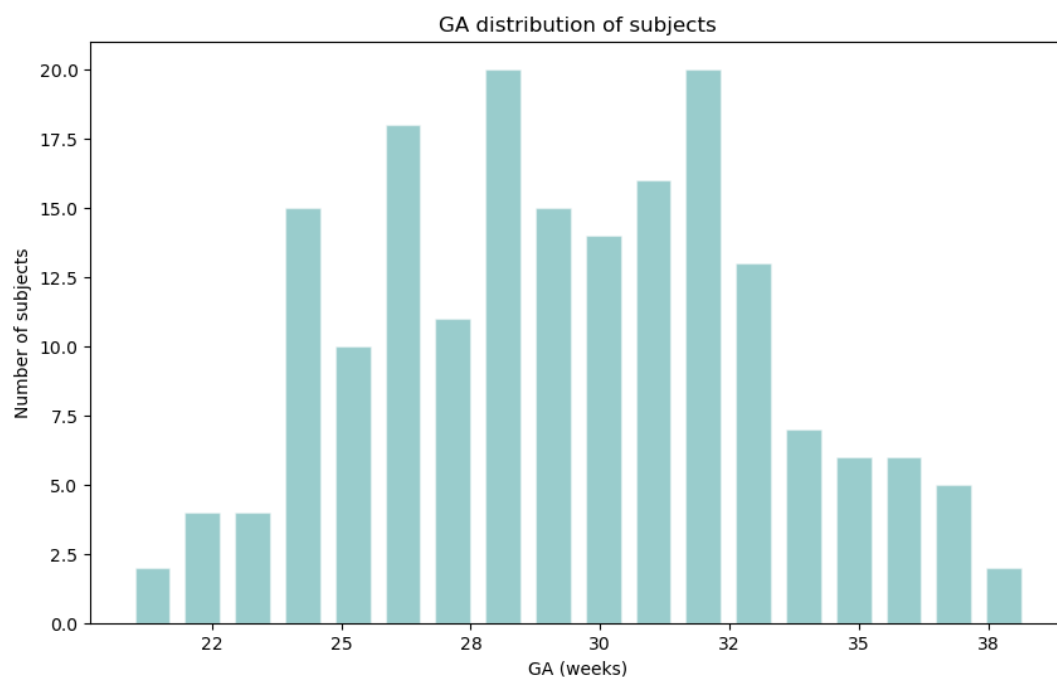


Figure 12: Histogram of fetal MRI dataset from dHCP showing the distribution of GAs.

The multimodal MRI dataset used in this project comprised 183 fetuses aged between 20 and 38 weeks of GA. Out of the 183 subjects, 6 were found to have incidental findings of VM, resulting in 177 healthy subjects and 6 with WM.

3.1.2 Diversity of data

There is growing evidence that medical AI models can be racially biased when trained on unbalanced datasets. Historically, racial, and ethnic minority groups have been underrepresented in existing biomedical datasets (39). This inherent bias may lead to inaccurate predictions and misdiagnoses (40). Therefore, it is crucial to assess the generalisability of healthcare AI algorithms across diverse demographics.

This is particularly important in the case of this project as studies have demonstrated that socioeconomic status can influence fetal brain development (41). EDI principles were not explicitly considered in this project, but it is worth noting that the dHCP dataset (2) used was collected at St. Thomas Hospital, reflecting the demographics of Lambeth and Greater London. However, certain demographics may be underrepresented in the dataset.

There is a possibility of microstructural variations in the fetal brain regions based on race/ethnicity and socioeconomic status so this represents an area for further investigation in future research.

3.2 Data acquisition

All in utero T2w and DWI images were acquired on a 3T Philips Achieva scanner with a 32-channel cardiac coil. Multiple single-shot turbo spin echo sequences with TE = 250 ms and TR = 2265 ms were used in the T2w acquisition process (42). This was followed by the reconstruction of the images to 0.5 mm isotropic resolution using an automated pipeline from Cordero-Grande et al. (36).

The DWI images were acquired using a combination of spin and field echo (SAFE) sequence at 2 mm isotropic resolution and multi-shell high angular resolution diffusion encoding – 15 volumes at $b = 0\text{s/mm}^2$, 46 volumes at $b = 400\text{s/mm}^2$, and 80 volumes at $b = 1000\text{s/mm}^2$ (36). Using a data-driven model of the spherical harmonics and radial decomposition (SHARD), HARDI datasets were reconstructed to 0.8 mm. The SHARD pipeline uses a slice-to-volume motion correction framework and dynamic distortion correction to handle subject motion in the data (43).

3.3 Diffusion modelling

The diffusion signal was modelled using the two techniques described in sections 1.3.2 and 1.3.3. Firstly, anisotropy and diffusivity components of the diffusion tensor are computed using the ‘tensor2metric’ command in MRtrix3 (5) resulting in FA and MD metrics from the HARDI data.

Secondly, Multi-shell multi-tissue constrained spherical deconvolution (MSMT-CSD) was used to extract fibre orientation density functions (fODFs) (29). This yielded the two other metrics – TF and FF.

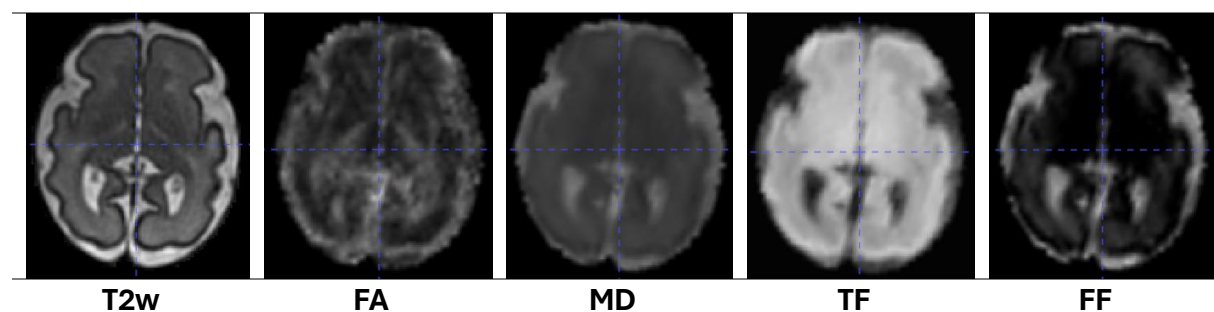


Figure 13: T2w image of a 30-week fetus along with the corresponding FA, MD, TF, and FF.

3.4 Data pre-processing

All T2w and diffusion maps were resized to have the dimensions 256 x 256 x 256 using the Medical Image Registration Toolkit (MIRTK) (44). Brain masks were applied to T2w and diffusion maps to remove non-brain regions using the NumPy library (45) in Python. All four diffusion maps (FA, MD, TF, and FF) for each subject were registered to the T2w space by rigid transformation (mapping using translations and rotations) using FMRIB Software Library (FSL) (4). This registration was necessary in preparation for obtaining labelled segmentation for the different transient brain regions.

3.4.1 Segmentation

Segmentation labels of the ROIs – CP, SP, WM, PVWM, and PZ (VZ and GE) were generated on the T2w images using an automated deep learning tissue parcellation tool from (3), which was pre-trained on the dHCP fetal dataset. As the diffusion maps were aligned to the T2w space, the segmentation labels could be automatically applied to FA, MD, TF, and FF as well.

The outcome of the pre-processing pipeline yielded aligned T2w, FA, MD, TF, and FF images for each subject, along with their corresponding labelled segmentations for all ROIs, prepared for feature extraction as shown in Figure 14.

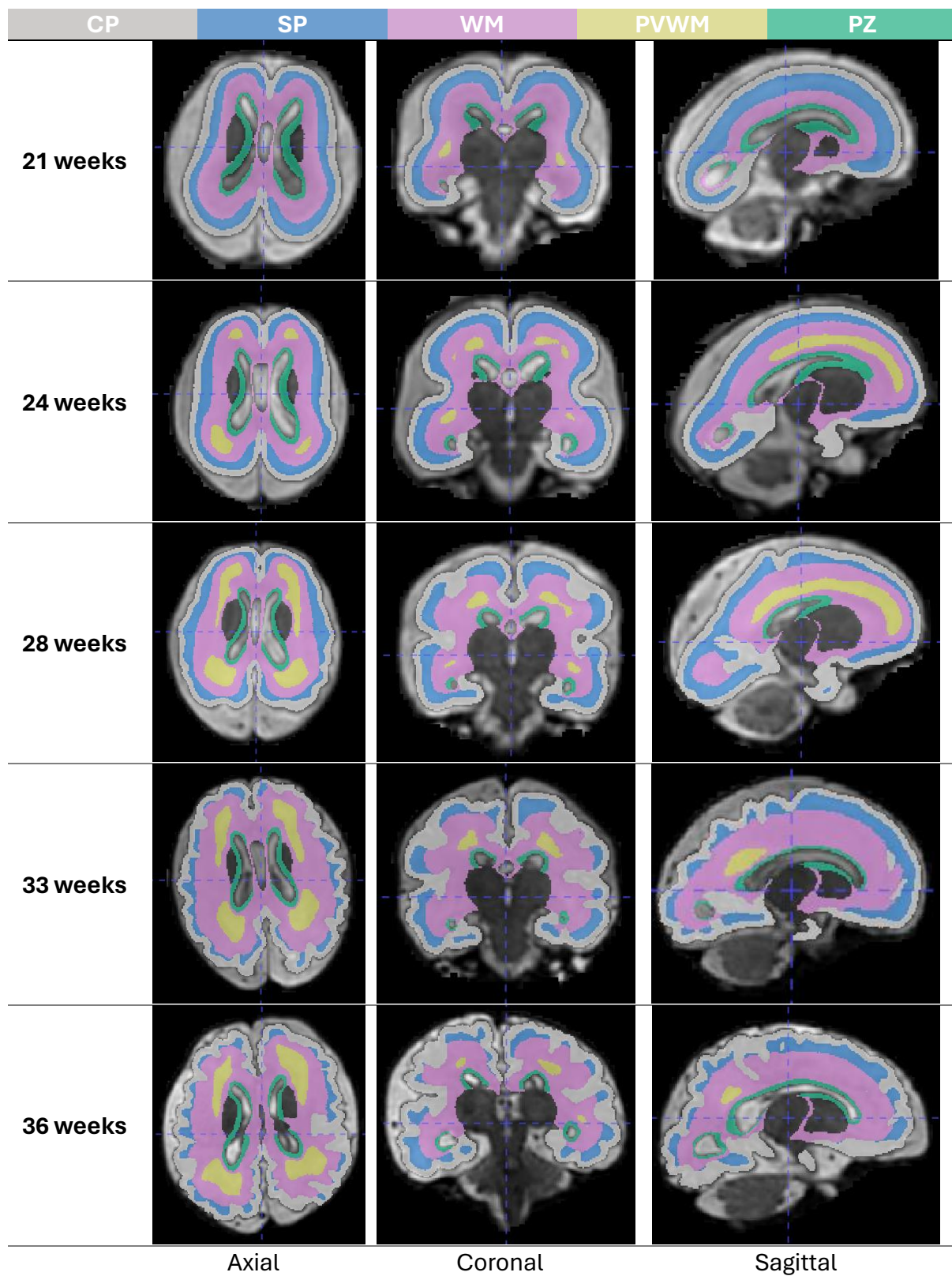


Figure 14: Axial, coronal, and sagittal views of five fetal subjects of 21, 24, 28, 33, and 36 GAs with the CP, SP, PZ, PVWM, and WM segmentation labels overlayed on their T2w images.

3.4.2 Feature extraction

After obtaining the labelled segmentations for the ROIs, these segmentations were multiplied with the four diffusion maps to extract the specific parts of the brain for each ROI. This allowed for the computation of the mean intensity value for each brain region across all diffusion maps. The outcome of this was a data frame containing the average regional values for each subject across every diffusion map for every ROI. This feature extraction was done using the NumPy library (45) in Python.

3.5 Polynomial ridge regression and model evaluation

Prior to model fitting, it was necessary to visualise how FA, MD, TF, and TF change across GA, so the average intensity values extracted in the previous step were plotted against GA. This preliminary step provided insight into the trends present and helped in determining what regression models would be appropriate to implement. It was apparent that the relationship between the diffusion metrics and GA is primarily non-linear. Furthermore, it was also evident that there was noise present in the data. This necessitated the implementation of a model that is equipped to handle non-linear relationships and effectively combat overfitting due to noise.

Polynomial ridge regression emerged as a suitable solution. Given that the main objective was to mitigate overfitting rather than focus on feature selection, ridge regularisation (L2) was deemed preferable over lasso regularisation (L1). To ensure consistency, a strategic approach was taken to select the optimal polynomial degree and alpha (L2 penalty) for each diffusion metric-GA relationship in every ROI. This was

accomplished through the use of hyperparameter tuning using cross-validation (CV).

The default scoring metric R^2 score was used as the scoring metric for CV.

This polynomial ridge regression pipeline was constructed using the scikit-learn library in Python (46). It included the following steps: polynomial feature transformation, standard scaling followed by ridge regression. Before the data could be processed through the pipeline, stratified sampling of the data was performed to ensure subjects with a representative range of GA were present in both the training (80%) and test (20%) sets.

Hyperparameter	Values					
Polynomial degree	1		2		3	
L2 penalty (λ)	0.001	0.01	0.1	1	10	100

Table 2: Hyperparameters used in cross validation.

The choice to include degree = 1 in the grid search for finding the best hyperparameters was made because it allows the pipeline to potentially select a simpler model if it performs better on the data. This was important due to the susceptibility of higher polynomial degrees to overfit to noise, particularly with larger datasets. For this reason, degrees higher than 3 were also not considered for evaluation based on the predominantly quadratic relationships observed within the data.

A 5-fold cross validation was performed on the model pipeline using the training set to determine the best combination of hyperparameters from the values shown in table 2. The model was fitted with the best hyperparameters ready to be validated on the test set. The model was evaluated by calculating the R^2 score. R^2 score was chosen as the evaluation metric as it is normalised and comparable between models and datasets.

Linear regression

It should be noted that polynomial ridge regression was implemented for all the diffusion metrics in all ROIs except for FA of the CP. This decision was made due to the linear relationship observed in the CP-FA data. Therefore, the Ordinary Least Squares (OLS) method of linear regression from the statsmodels module (47) in Python was employed. The linear relationship was confirmed through the calculation of the p-value of the linear model coefficient.

3.6 Analysis of VM subjects

The next step in the process was to identify any abnormalities present in subjects with VM. To assess this, z-scores of the average regional values were calculated and visualised. Z-scores indicate how many standard deviations from the mean of the dataset a data point lies. It is calculated by subtracting the mean (μ) of the dataset from the data point (x) and dividing by the standard deviation (σ) as shown in equation 4.

$$Z = \frac{x - \mu}{\sigma} \quad (4)$$

Equation 4: Formula for calculating z-scores where x denotes the data point, μ denotes the mean and σ denotes the standard deviation.

Before the z-scores were calculated, the dataset was categorised into the respective GA groups based on the number of weeks. This was done so that VM subjects could be compared to healthy subjects of the same GA. Secondly, the z-scores of each GA group were computed and the z-scores of the VM subjects were extracted. To facilitate comparative analysis with healthy subjects, z-scores of the healthy subjects were also calculated for each GA group. However, this step was done with the exclusion of VM

subjects in order to establish a normative reference. These calculations were done using the stats module from the SciPy library (48) in Python.

Finally, the results were visualised using boxplots to compare z-scores of VM and healthy subjects across all GAs.

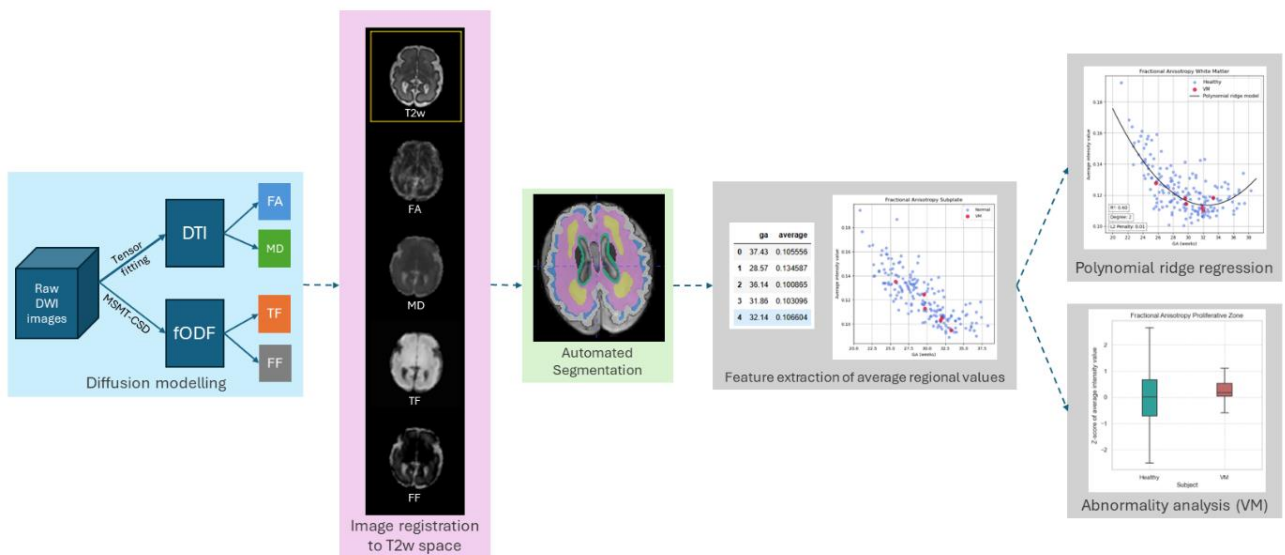


Figure 15: Summarised pipeline of methodology.

4 RESULTS

Overview of results

The overall observed trends in FA, MD, TF, and FF across all ROIs seen in Figures 16, 17, 18, 19, 20, and 21 will be outlined before presenting the results.

Overall, FA of all the ROIs show a decreasing trend with GA. With the exception of WM, where FA starts to increase during late gestation at ~ 32 GA. This suggests that as the fetal brain develops, the water movement in most transient regions becomes less directional.

TF on the other hand, displays U-shaped trends for most ROIs. It can be seen that there is an initial declining trajectory followed by an increase at various points in GA for different regions. Except in CP, where TF remains steady in its upward progression throughout GA. The U-shaped trend indicates an initial reduction in tissue density followed by an increase with maturation.

MD and FF demonstrate comparable inverted U-shaped trends, though they contrast TF in their dynamics. Both MD and FF show an initial increase, reaching a peak at specific GAs before beginning to decline. This suggests that water content peaks during mid to late gestation before the diffusion rate starts to slow down towards the end.

Interestingly, FA and TF do not always follow similar trends. This contradiction could indicate a high volume of crossing fibres in these regions.

	Whole brain	CP	SP	WM	PZ
FA	Steady decline until ~34 GA, at which point starts to plateau	Steady decline throughout	Steady decline until ~34 GA, at which point starts to plateau	Gradual decrease until ~32 GA, at which point starts to increase	No identifiable trend
				IP: ~32 GA	
MD	Gradual increase until ~28 GA, at which point starts to decrease	Gradual increase until ~27 GA, at which point starts to decrease	Gradual increase until ~28 GA, at which point starts to decrease	Gradual increase until ~29 GA, at which point starts to decrease	Gradual increase until ~31 GA, at which point starts to decrease
	IP: ~28 GA	IP: ~27 GA	IP: ~28 GA	IP: ~29 GA	IP: ~31 GA
TF	Gradual decrease until ~28 GA, at which point starts to increase	Gradual increase until ~27 GA at which point starts to increase at a faster rate	Gradual decrease until ~28 GA, at which point starts to increase	Gradual decrease until ~29 GA, at which point starts to increase	Gradual decrease until ~31 GA, at which point starts to increase
	IP: ~28 GA		IP: ~28 GA	IP: ~29 GA	IP: ~31 GA
FF	Gradual increase until ~28 GA, at which point starts to decrease	Slight increase initially but starts to steadily decline at ~27 GA	Gradual increase until ~28 GA, at which point starts to decrease	Gradual increase until ~29 GA, at which point starts to decrease	Gradual increase until ~31 GA, at which point starts to decrease
	IP: ~28 GA		IP: ~28 GA	IP: ~29 GA	IP: ~31 GA

Table 3: Summary of observed trends in FA, MD, TF, and FF across all ROIs. In regions where a change of trajectory was observed, the GA at the inflection point (IP) has been identified.

4.1 Polynomial ridge regression model

To begin with, diffusion metrics of the whole brain which includes all brain tissue excluding the ventricles and CSF are shown in Figure 16. This is to gain an understanding of the overall trends present in the fetal brain during gestation to allow for a clear distinction of how the individual transient structures develop compared to the entire brain.

In Figure 16, it can be seen that FA decreases with GA. This shows that the overall directionality of diffusion in all brain tissue reduces with GA suggesting that the water movement becomes less directional as the brain develops. On the other hand, MD and FF exhibit similar relationships where they both increase up until ~28 GA at which point

they start to decrease. This implies that the average water diffusion (regardless of direction) is high until ~28 GA when it starts to decline.

TF exhibits an inverse relationship to MD and FF as it decreases up until ~28 GA at which point it starts to increase.

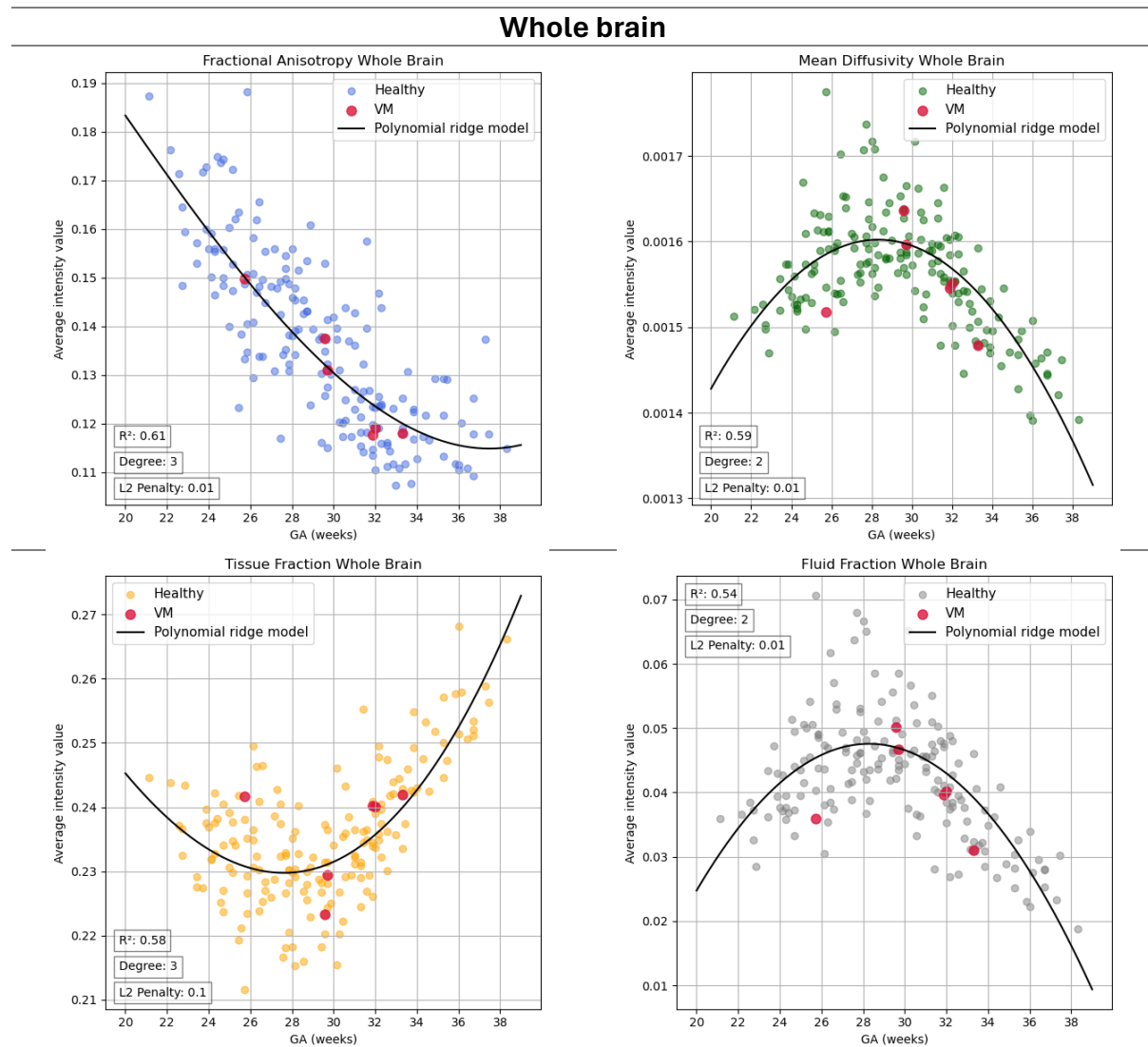


Figure 16: Four polynomial ridge models showing FA, MD, TF, and FF of the whole brain vs GA along with the polynomial degree and L2 penalty chosen by the cross-validation. The train set R^2 score of each model is also shown on the plots. VM subjects are highlighted in red.

What is interesting is that FA of the CP is the only metric that presents a linear trend steadily decreasing with GA. The linearity of FA was confirmed with the p-value as shown in Figure 17. The low p-value shows that the linear relationship is statistically

significant. MD shows an upward trend at the start, peaks at ~27 GA and declines thereafter. FF shows a slight increase at the beginning but also starts declining at ~27 GA. It should be noted that TF of the CP is the only TF that does not exhibit a U-shaped curve as it has a steady upward progression with GA.

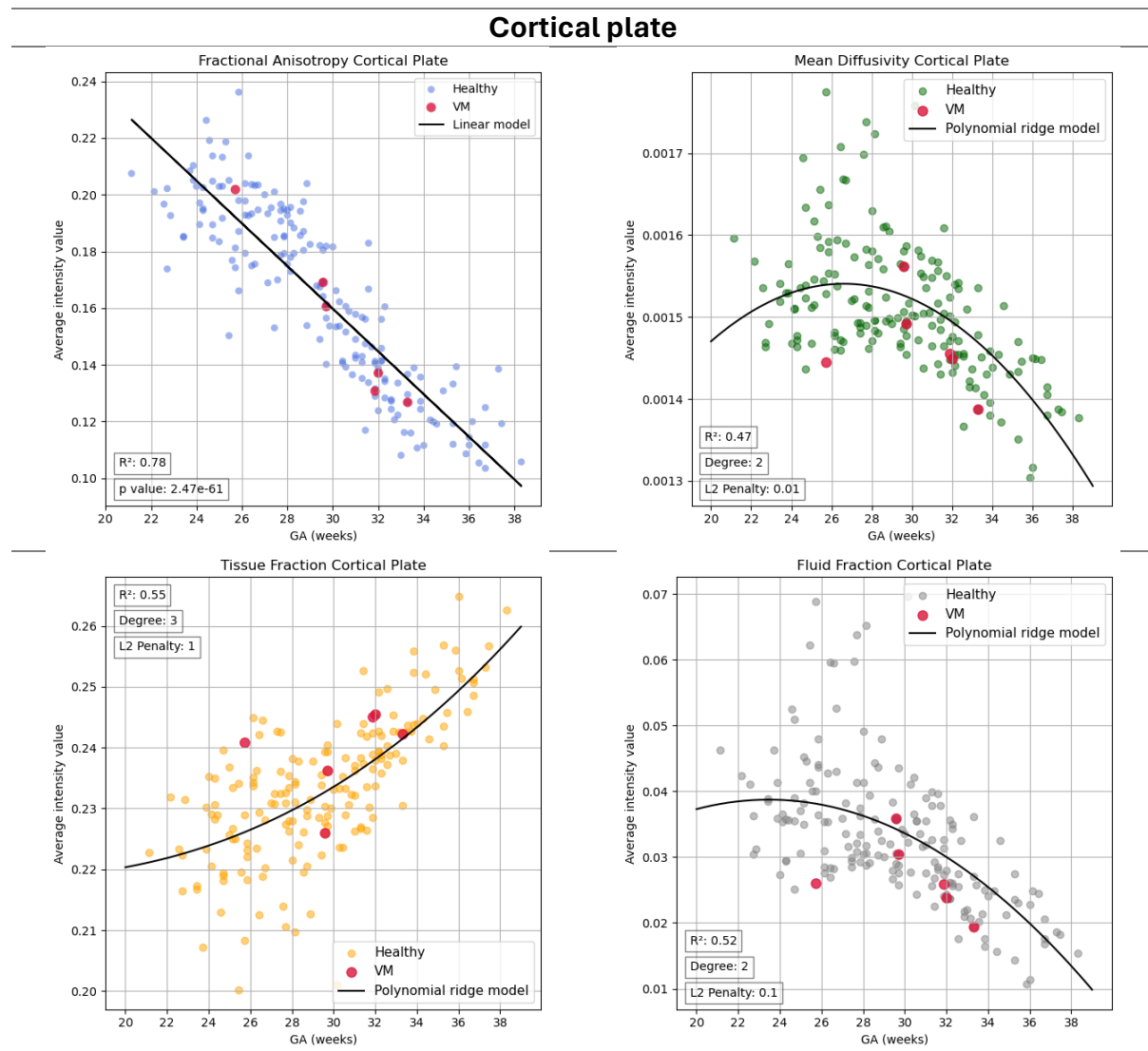


Figure 17: Four polynomial ridge models showing FA, MD, TF, and FF of the CP vs GA along with the polynomial degree and L2 penalty chosen by the cross-validation. The train set R² score of each model is also shown on the plots. VM subjects are highlighted in red.

SP demonstrates a very similar trend to the whole brain where FA decreases with GA but levels off at the end at ~34 GA which is also the same time FA of the whole brain starts

to plateau. MD and FF both rise and fall peaking at ~28 GA. TF however shows an inverse relationship to MD and FF as it falls and rises with a trough at ~28 GA.

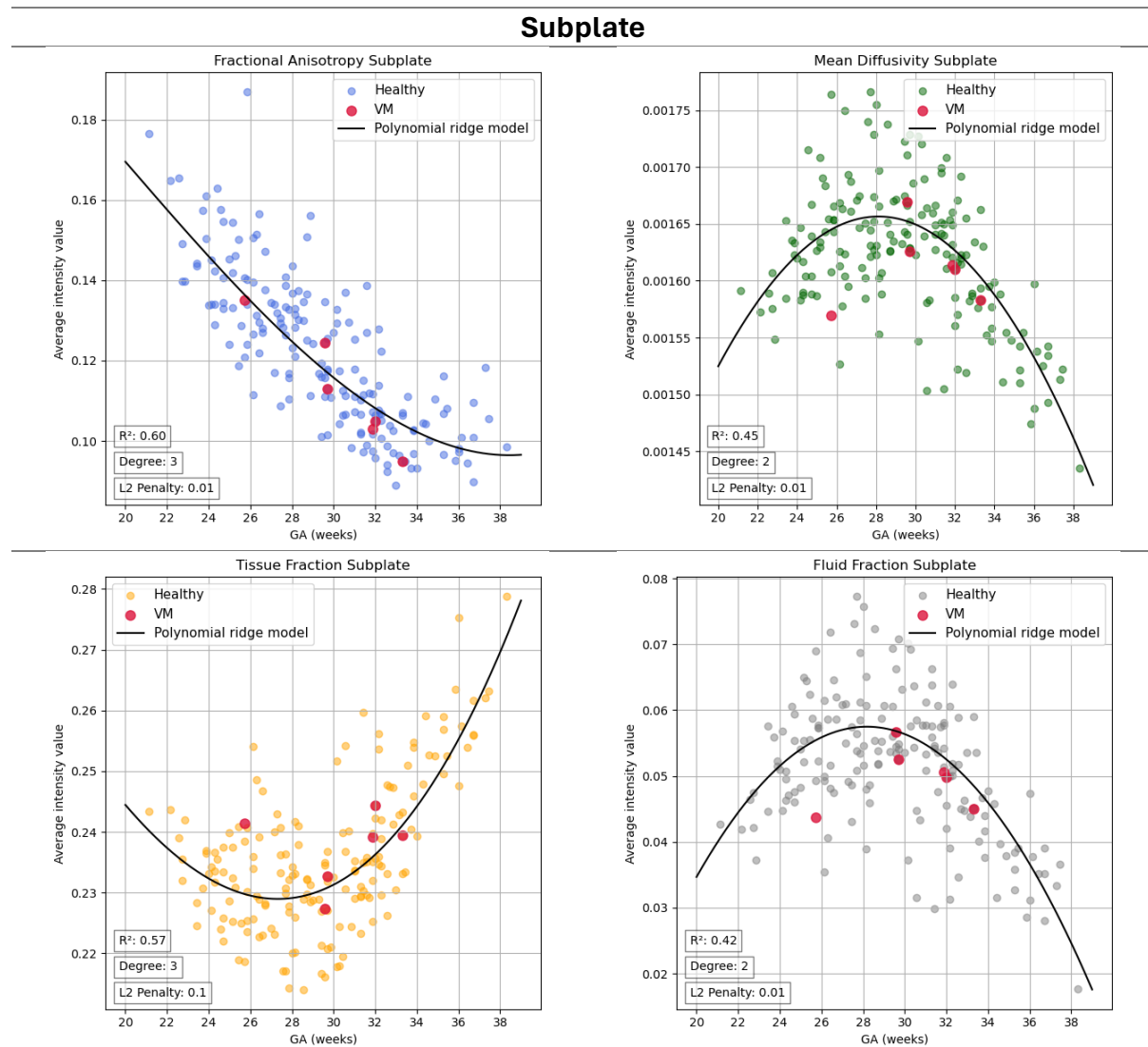


Figure 18: Four polynomial ridge models showing FA, MD, TF, and FF of the SP vs GA along with the polynomial degree and L2 penalty chosen by the cross-validation. The train set R^2 score of each model is also shown on the plots. VM subjects are highlighted in red.

FA of WM shows a downward trend until ~32 GA, after which it begins to increase. Both MD and FF present inverted U-shaped curves peaking at ~29 GA. TF exhibits an inverse relationship to MD and FF with a U-shaped curve and a trough at ~29 GA.

White matter

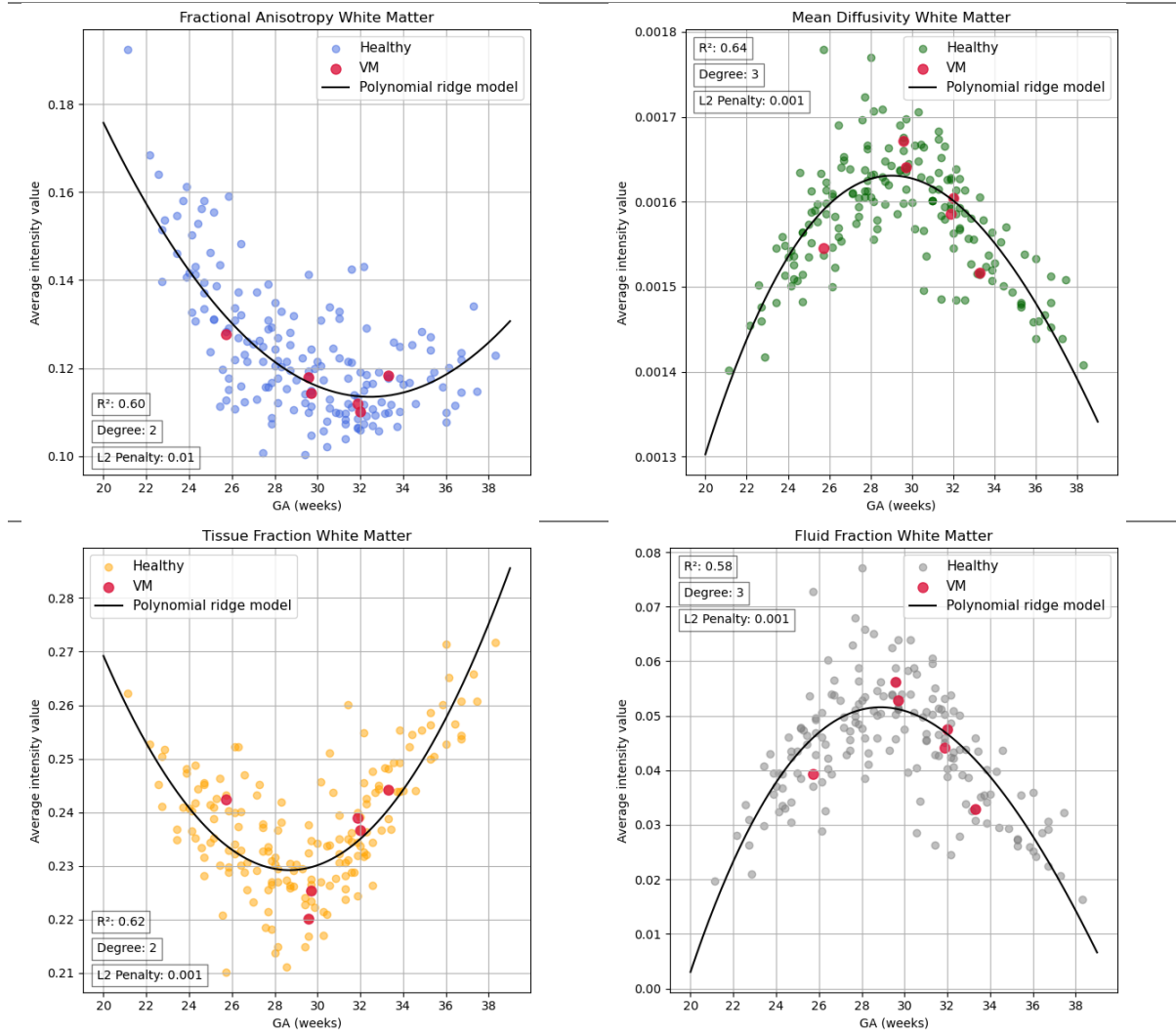


Figure 19: Four polynomial ridge models showing FA, MD, TF, and FF of the WM vs GA along with the polynomial degree and L2 penalty chosen by the cross-validation. The train set R^2 score of each model is also shown on the plots. VM subjects are highlighted in red.

FA of the PZ is the only diffusion metric where no identifiable trend was found by the model. As seen in Figure 20, no visual correlation is observed. To investigate this further, FA of GE is shown separately in Figure 21, where FA decreases with GA. This suggests that the issue may lie with the FA of the VZ. MD and FF both increase until ~31 GA where they start to decline. TF demonstrates a U-shaped curve with an inflection point at ~31 GA where TF starts to rise.

Proliferative zone

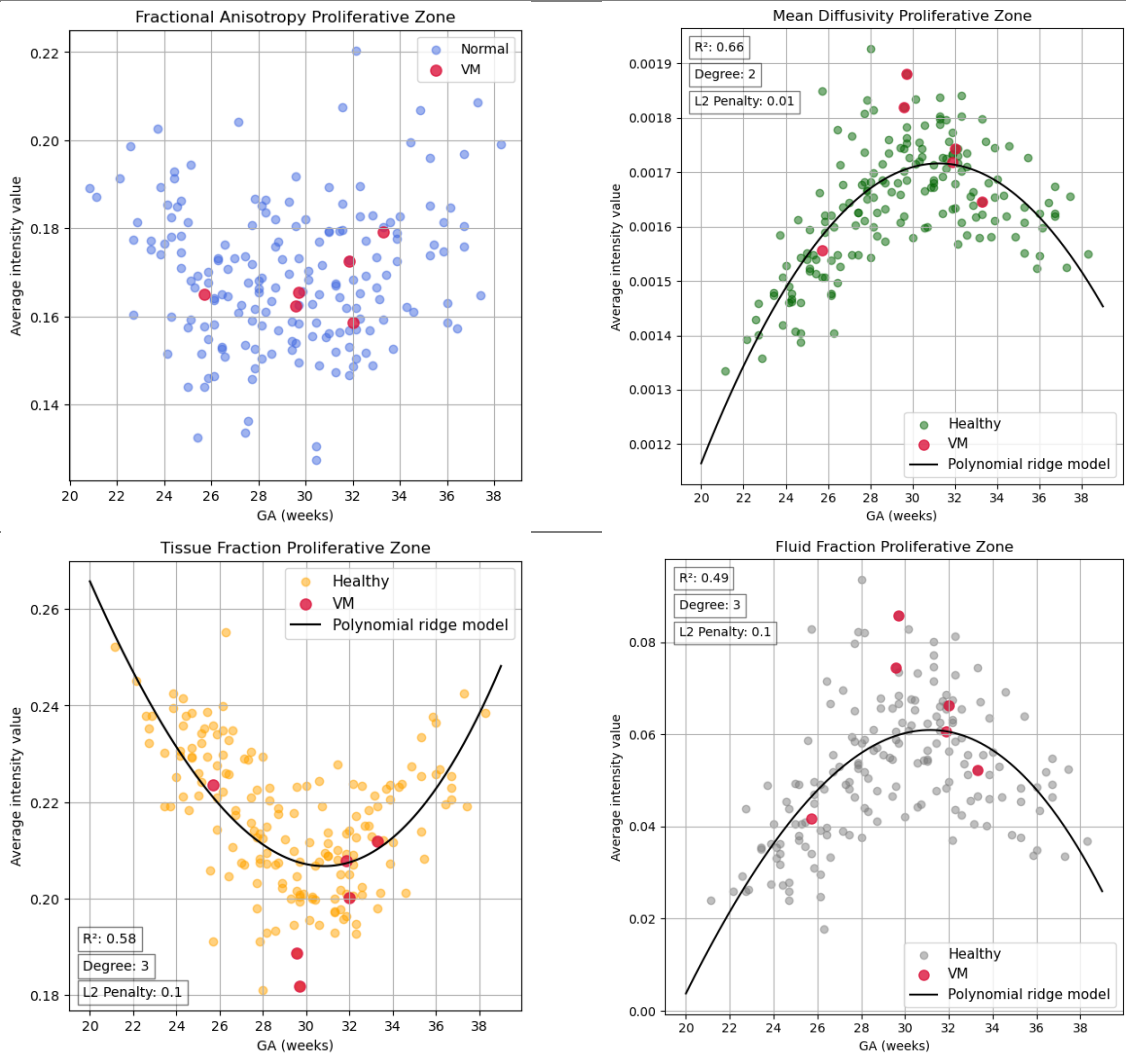


Figure 20: Three polynomial ridge models showing MD, TF, and FF of the PZ vs GA along with the polynomial degree and L2 penalty chosen by the cross-validation. Scatter plot of FA shown as no suitable model was found. The train set R^2 score of each model is also shown on the plots. VM subjects are highlighted in red.

Ganglionic eminence

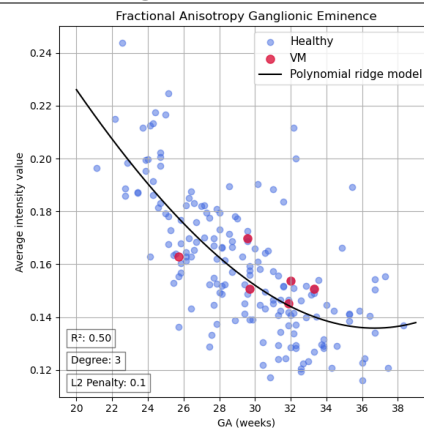


Figure 21: Polynomial ridge model of FA of the GE vs GA along with the polynomial degree and L2 penalty chosen by the cross-validation. The train set R^2 score of the model is also shown on the plot. VM subjects are highlighted in red.

As it can be seen in Figures 16, 17, 18, 19, 20 and 21, VM subjects do not appear as outliers and seem to present normative trends. This was further analysed using statistical measures, the results of which are discussed in section 4.3.

4.2 Model evaluation

	Whole brain	CP	SP	WM	PZ
FA	0.61	0.78	0.60	0.60	
	0.55	0.71	0.57	0.54	
MD	0.59	0.47	0.45	0.64	0.66
	0.46	0.30	0.40	0.54	0.51
TF	0.58	0.55	0.57	0.62	0.58
	0.50	0.48	0.51	0.55	0.43
FF	0.54	0.52	0.42	0.58	0.49
	0.41	0.31	0.39	0.49	0.37

Table 4: Comparison of R^2 scores of train and test sets for all models. Train set scores are shaded in grey with test set scores below them.

Polynomial ridge regression consistently performed the best on FA as evident by the R^2 scores in Table 4.

FA of CP has the highest R^2 score on both train and test sets. However, this is not a polynomial ridge regression model. It is a linear regression model.

It is evident that polynomial ridge regression is an informative model for understanding the relationship between input features (GA) and target variables (diffusion metrics). These models have facilitated the identification of correlations between data trends present in the diffusion data and neurobiological processes in the brain. However, as shown in Table 4, all R^2 scores on the train sets of ridge regression are below 0.66, with the lowest score being 0.42. This indicates that the noise in the diffusion data may be affecting the model accuracies despite the use of regularisation.

4.3 Analysis of VM subjects

The analysis of VM subjects did not yield conclusive results. The z-scores of VM subjects did not consistently vary significantly from the healthy subjects, making it difficult to establish any deviations from healthy subjects at this stage.

However, some of the box plots exhibited noteworthy findings, which are displayed in Figure 22. The remaining box plots can be found in the appendix as supplementary materials.

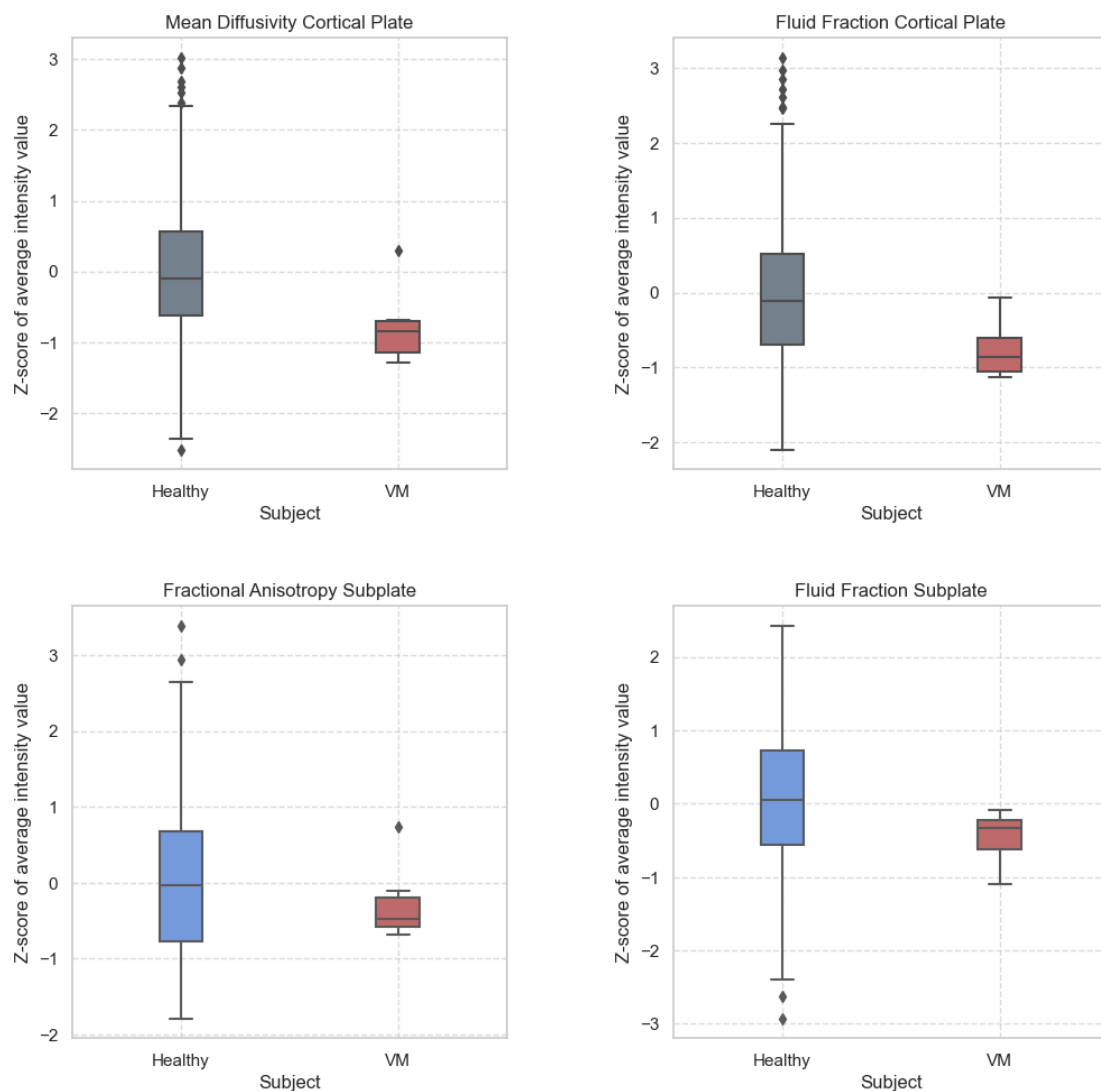


Figure 22: Box plots of CP - MD, FF, and SP - FA, FF comparing the z-scores of healthy and VM subjects.

Upon analysis of the results in Figure 22, it is evident that the VM subjects exhibit negative z-scores in MD and FF of the CP and FA and FF of the SP. This suggests that VM subjects may present with lower MD and FF values in the CP and lower FA and FF values in the SP when compared to healthy subjects of similar GA.

In the box plots, it was observed that a few healthy subjects and VM subjects appeared as outliers in certain plots. However, the same subjects did not consistently appear as outliers, rendering this information arbitrary. This presence of healthy subjects as outliers can be attributed to data noise and varying image quality.

5 DISCUSSION

The results presented in section 4 outlined the observed trends among FA, MD, TF, and FF in the ROIs. In this section, the correlations between the trends and the underlying neurobiology will be discussed, highlighting the key findings of the project.

5.1 Analysis of results

CP presents with a linearly decreasing FA in relation to GA. This phenomenon can be attributed to the ongoing neuronal migration from the PZ to the CP during the early stages of the second trimester. This leads to the presence of radial glia in the CP. This radial arrangement of the cells may hinder the movement of water perpendicular to the cortical surface more than in the radial direction (49), resulting in high anisotropy at the beginning. However, as neurons mature and establish connections, this radial organisation may become disrupted (49), leading to a reduction in anisotropy and subsequently a decrease in FA as seen in Figure 17.

Figure 17 also shows that MD and FF of CP decrease with GA, while TF increases. This observation can be clarified as during the early stages of the third trimester, cortical maturation is primarily dominated by a rise in cellular and organelle density (50). This accounts for the increase in tissue volume and the reduction in fluid and diffusivity.

TF can be seen increasing with GA over the third trimester in all the regions whereas FF displays contrasting behaviour. This reflects the developing fetal cytoarchitecture as neuronal maturation results in reduction of extracellular water (51).

As tissue volume increases, there is an expected increase in the directional flow of water. However, all the regions exhibit a decrease in FA indicating a decrease in the directionality of water movement. This could be attributed to the fact that the presence of crossing fibres may be impacting the interpretation of FA.

The trend seen in TF of the SP in Figure 18 can be explained by the fact that from 32 GA onwards, the SP starts to diminish and its location is taken up by the emerging white matter (52). This correlates to the rapidly increasing TF in late gestation seen in Figure 18.

One significant discovery from the results, as presented in Table 3, is that the water content and diffusivity reach their peak in all regions at similar GAs. The whole brain, CP, SP, and WM have inflection points in MD and FF at ~28/29 GA, while PZ has its inflection points a bit later at ~31 GA. The exact neurobiological process behind this pattern is difficult to pinpoint at this stage, but this intriguing finding poses a quest for further investigation.

As seen in Figure 20, there is no discernible correlation between FA of the PZ and GA. However, as seen in Figure 21, FA of GE displays a downward trend, consistent with the findings in FA of other ROIs. This anomaly may be attributed to the greater thickness of the GE compared to the VZ, both of which comprise the PZ as mentioned in section 1.2.4. Consequently, the accuracy of segmentations in the VZ region may be compromised due to lower resolution and noise levels. However, the reasons for the observable trends in MD, TF, and FF of PZ remain unclear.

It is commonly known that real world data is subject to noise and imperfections. Even when the model is finely tuned and its hyperparameters are optimised, and the model

appears to visually fit the data, it may still result in a low R^2 score if the data contains inherent noise. However, despite this challenge, due to the regularisation technique implemented, the models were able to combat overfitting and did not demonstrate significantly poorer performance on test sets compared to training sets as seen in Table 4 indicating its ability to generalise well to unseen data. The low R^2 scores can be attributed to the presence of noise in the data rather than a deficiency in the model's performance, as evidenced by the consistent scores between training and test sets.

5.2 Comparison to the state of art

The average FA, MD, TF, and FF intensity values of CP and SP are similar to those reported by Wilson et al. (36) whose study examined the diffusion metrics in those two regions.

As detailed in the results, the FA of the CP did not plateau like in the SP and whole brain. It demonstrates a steady linear decrease with GA. This correlates to the findings by Calixto et al. (35) who found that there was no deceleration of FA in the CP.

Additionally, it should be noted that (35) utilised the median values of FA and MD whereas this project calculated the mean values. Median values would provide insight into the central tendency of FA and MD compared to mean values which give representations of the overall trend.

Furthermore, the FA trends seen in the whole brain, CP and SP are similar to the trends found by (35). In some cases, there are discrepancies in trends observed between this study and theirs. This can be attributed to the variations in the GAs of the subjects used. Their study included subjects with GAs ranging from 23 to 36 weeks. As a result, certain

trends observed in either extreme of GA which were captured by our model are not accounted for in (35). An example of this scenario is shown in Figure 23 where the trends seen after 32 GA in the results from this project are not observed in the plots from their work.

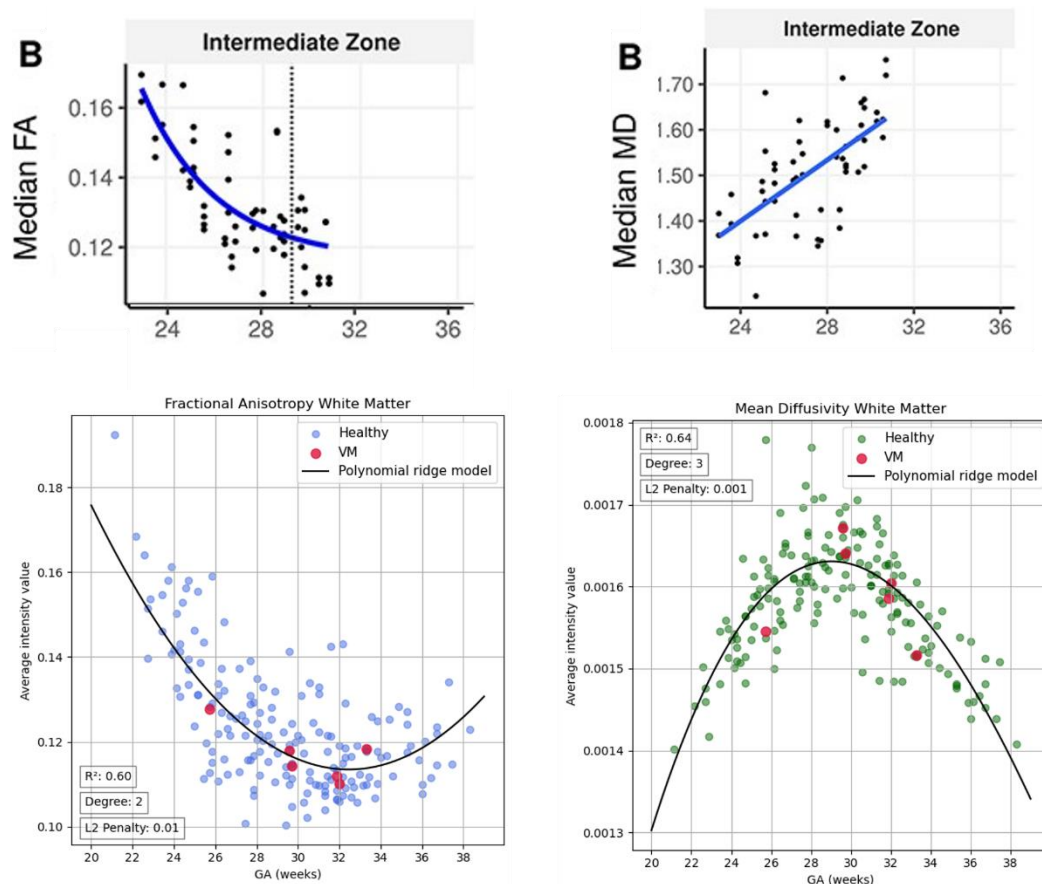


Figure 23: Comparison of FA and MD of WM/ IZ between results from Calixto et al. and results from this project. Top two plots taken from (35).

Despite the discrepancies observed at extreme GAs, the trends of FA and MD identified in the outcomes of this study exhibit comparability with those reported by (35). The primary distinction lies in the characterisation of certain models as linear by (35), whereas the regression models employed in this study identify them as non-linear. This divergence may stem from the larger sample size utilised in this study compared to

theirs, which was limited to 44 fetuses. The larger dataset in this study potentially enhances the model's capability to discern underlying relationships more accurately.

Lastly, (36) conducted an analysis of FA, MD, TF, and FF in two of the regions included in this study. In contrast, (35) examined all regions but focused solely on FA and MD.

5.3 Limitations

The project was constrained by the small number of VM subjects being investigated, comprising of only 6 cases. This limitation resulted in an insufficient amount of data to identify any statistically significant deviations or establish conclusive evidence of microstructural abnormalities within the fetal transient layers in fetuses with VM.

Furthermore, the feature extraction treated both hemispheres as a whole, overlooking potential asymmetries that are known to be inherent in VM cases. This oversight may have masked any subtle differences in the microstructure leading to the lack of significant difference between VM and healthy subjects.

6 CONCLUSION

The findings from this project reveal a novel perspective on the two other diffusion metrics TF and FF which have previously not been analysed extensively in specific brain regions targeted by this study. While normative trends of healthy subjects have been identified, additional research with a larger sample size of VM subjects is needed to verify any deviations from the norm caused by VM. One of the major findings to emerge from this study is that the fluid content in the fetal brain appears to reach its peak at specific GAs across all ROIs before starting to decline in late gestation. This information has not been definitively established in existing literature. In conclusion, the insights gained from this study advance the understanding of early neurodevelopmental trajectories. This knowledge holds promise for potentially informing the diagnosis and management of fetal brain abnormalities in the future, contributing to both clinical practice and socioeconomic development.

6.1 Future work

In the analysis of VM subjects, both hemispheres of the brain were evaluated together. However, given the nature of VM as a condition which is characterised by one ventricle being abnormally larger than the other, it would be more appropriate to consider the hemispheres separately when calculating z-scores. This alternative approach may reveal any deviations between the two sides and provide a better in-depth contextual analysis.

Additionally, future work would include the investigation of the ability of polynomial ridge regression in predicting the GA given diffusion metrics and assess which diffusion

metric allows for the most accurate predictions of GA. Furthermore, any inaccurate predictions of GA could potentially be used to identify subjects with abnormal brain development.

Finally, it would be beneficial to graph the rate of change for the diffusion metrics as (35) have done. This could provide insight into the pace at which microstructural changes are taking place in the transient regions.

7 REFERENCES

1. Vasung L, Abaci Turk E, Ferradal SL, Sutin J, Stout JN, Ahtam B, et al. Exploring early human brain development with structural and physiological neuroimaging. *NeuroImage*. 2019 Feb 15;187:226–54.
2. The Developing Human Connectome Project [Internet]. [cited 2024 Apr 15]. Available from: <https://www.developingconnectome.org/>
3. Sousa HS, Fukami-Gartner A, Uus AU, Kyriakopoulou V, Ziukaite B, Anzak I, et al. A Deep Learning Approach for Segmenting the Subplate and Proliferative Zones in Fetal Brain MRI. In: Perinatal, Preterm and Paediatric Image Analysis: 8th International Workshop, PIPPI 2023, Held in Conjunction with MICCAI 2023, Vancouver, BC, Canada, October 12, 2023, Proceedings [Internet]. Berlin, Heidelberg: Springer-Verlag; 2023 [cited 2024 Apr 15]. p. 17–27. Available from: https://doi.org/10.1007/978-3-031-45544-5_2
4. FSL - FslWiki [Internet]. [cited 2024 Apr 21]. Available from: <https://fsl.fmrib.ox.ac.uk/fsl/fslwiki>
5. MRtrix3 [Internet]. [cited 2024 Apr 23]. Available from: <https://www.mrtrix.org/>
6. GPy by SheffieldML [Internet]. [cited 2024 Apr 23]. Available from: <https://sheffieldml.github.io/GPy/>
7. Stiles J, Jernigan TL. The Basics of Brain Development. *Neuropsychol Rev*. 2010;20(4):327–48.
8. Rasband MN. Glial Contributions to Neural Function and Disease. *Mol Cell Proteomics MCP*. 2016 Feb;15(2):355–61.
9. Sontheimer H. Chapter 11 - Neurodevelopmental Disorders. In: Sontheimer H, editor. *Diseases of the Nervous System* [Internet]. San Diego: Academic Press; 2015 [cited 2024 Apr 16]. p. 319–47. Available from: <https://www.sciencedirect.com/science/article/pii/B9780128002445000112>
10. Kostović I, Sedmak G, Judaš M. Neural histology and neurogenesis of the human fetal and infant brain. *NeuroImage*. 2019 Mar 1;188:743–73.
11. Vasung L, Lepage C, Radoš M, Pletikos M, Goldman JS, Richiardi J, et al. Quantitative and Qualitative Analysis of Transient Fetal Compartments during Prenatal Human Brain Development. *Front Neuroanat*. 2016;10:11.
12. ScienceDirect.com | Science, health and medical journals, full text articles and books. [Internet]. [cited 2024 Apr 26]. Available from: <https://www.sciencedirect.com/>

13. Yu Q, Ouyang A, Chalak L, Jeon T, Chia J, Mishra V, et al. Structural Development of Human Fetal and Preterm Brain Cortical Plate Based on Population-Averaged Templates. *Cereb Cortex* N Y NY. 2016 Oct;26(11):4381–91.
14. Rados M, Judas M, Kostović I. In vitro MRI of brain development. *Eur J Radiol*. 2006 Feb;57(2):187–98.
15. Wilson S, Pietsch M, Cordero-Grande L, Christiaens D, Uus A, Karolis VR, et al. Spatiotemporal tissue maturation of thalamocortical pathways in the human fetal brain. *eLife*. 12:e83727.
16. Stuempflen M, Taymourtash A, Kienast P, Schmidbauer VU, Schwartz E, Mitter C, et al. Ganglionic eminence: volumetric assessment of transient brain structure utilizing fetal magnetic resonance imaging. *Ultrasound Obstet Gynecol*. 2023;62(3):405–13.
17. Prayer D, Brugger PC, Prayer L. Fetal MRI: techniques and protocols. *Pediatr Radiol*. 2004 Sep;34(9):685–93.
18. Ahn S, Lee SK. Diffusion Tensor Imaging: Exploring the Motor Networks and Clinical Applications. *Korean J Radiol Off J Korean Radiol Soc*. 2011 Nov 1;12:651–61.
19. Debnam JM, Schellingerhout D. Diffusion MR Imaging of the Brain in Patients with Cancer. *Int J Mol Imaging*. 2011;2011:714021.
20. O'Donnell LJ, Westin CF. An introduction to diffusion tensor image analysis. *Neurosurg Clin N Am*. 2011 Apr;22(2):185–viii.
21. Mori S, Tournier JD, editors. Chapter 8 - Moving Beyond DTI: High Angular Resolution Diffusion Imaging (HARDI). In: *Introduction to Diffusion Tensor Imaging (Second Edition)* [Internet]. San Diego: Academic Press; 2014 [cited 2024 Apr 25]. p. 65–78. Available from:
<https://www.sciencedirect.com/science/article/pii/B9780123983985000084>
22. Tournier JD, Mori S, Leemans A. Diffusion Tensor Imaging and Beyond. *Magn Reson Med*. 2011 Jun;65(6):1532–56.
23. Kotian RP, Koteshwar P. Fractional Anisotropy: Scalar Derivative of Diffusion-Tensor Imaging. In: Kotian RP, Koteshwar P, editors. *Diffusion Tensor Imaging and Fractional Anisotropy: Imaging Biomarkers in Early Parkinson's Disease* [Internet]. Singapore: Springer Nature; 2022 [cited 2024 Apr 5]. p. 59–84. Available from:
https://doi.org/10.1007/978-981-19-5001-8_5
24. Rouine J, Callaghan CK, O'Mara SM. Chapter 6 - Opioid modulation of depression: A focus on imaging studies. In: O'Mara S, editor. *Progress in Brain Research* [Internet]. Elsevier; 2018 [cited 2024 Apr 5]. p. 229–52. (The Opioid System as the Interface between the Brain's Cognitive and Motivational Systems; vol. 239). Available from:
<https://www.sciencedirect.com/science/article/pii/S0079612318301134>

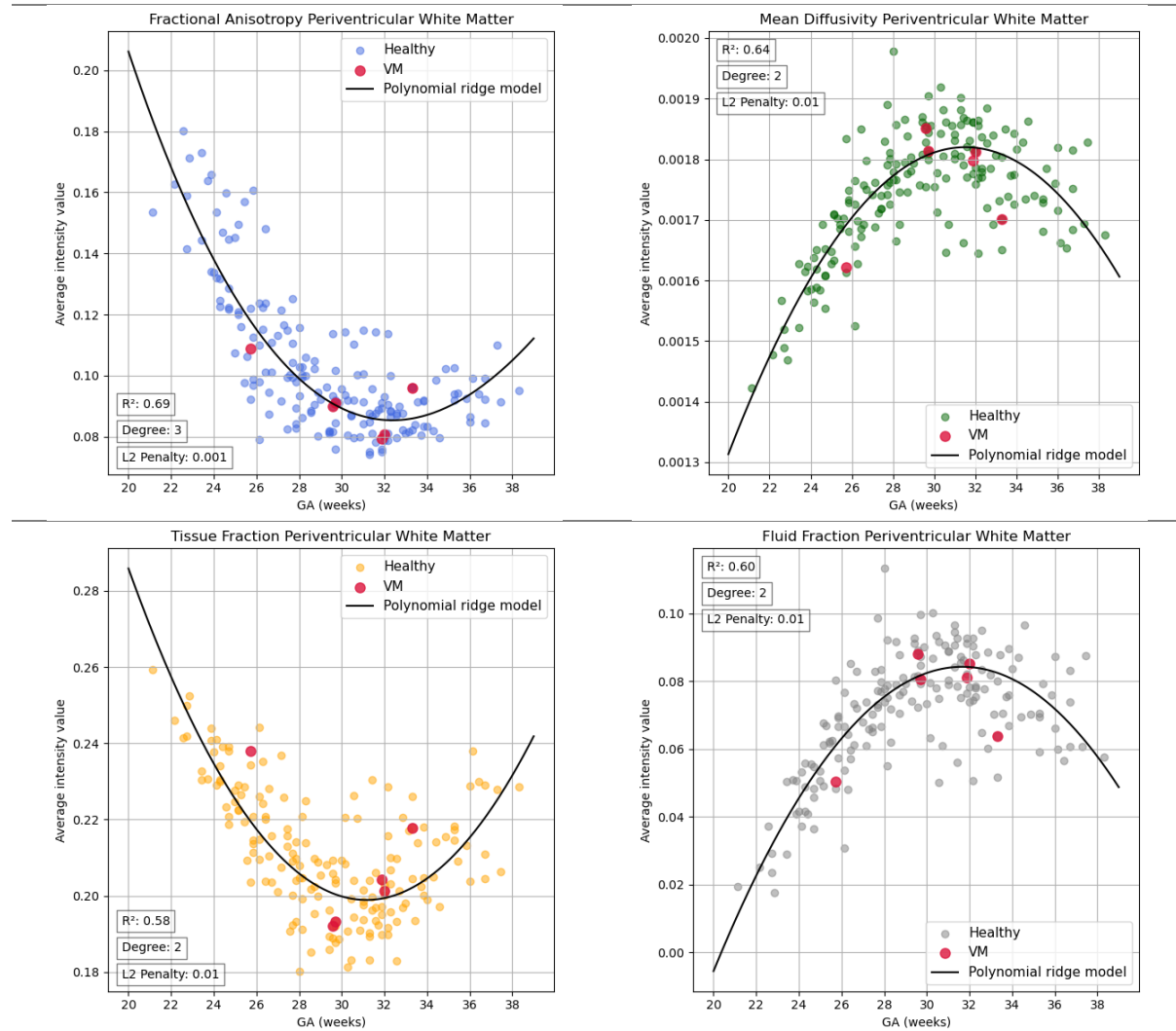
25. Questions and Answers in MRI [Internet]. [cited 2024 Apr 25]. DTI. Available from: <http://mriquestions.com/dti-tensor-imaging.html>
26. Salat DH. Chapter 12 - Diffusion Tensor Imaging in the Study of Aging and Age-Associated Neural Disease. In: Johansen-Berg H, Behrens TEJ, editors. Diffusion MRI (Second Edition) [Internet]. San Diego: Academic Press; 2014 [cited 2024 Apr 15]. p. 257–81. Available from: <https://www.sciencedirect.com/science/article/pii/B9780123964601000123>
27. Stebbins GT. Diffusion Tensor Imaging in Parkinson's Disease. In: Kompoliti K, Metman LV, editors. Encyclopedia of Movement Disorders [Internet]. Oxford: Academic Press; 2010 [cited 2024 Apr 5]. p. 308–10. Available from: <https://www.sciencedirect.com/science/article/pii/B9780123741059000204>
28. Lenglet C, Campbell JSW, Descoteaux M, Haro G, Savadjiev P, Wassermann D, et al. Mathematical methods for diffusion MRI processing. *NeuroImage*. 2009 Mar 1;45(1, Supplement 1):S111–22.
29. Jeurissen B, Tournier JD, Dhollander T, Connelly A, Sijbers J. Multi-tissue constrained spherical deconvolution for improved analysis of multi-shell diffusion MRI data. *NeuroImage*. 2014 Dec 1;103:411–26.
30. Pietsch M, Christiaens D, Hutter J, Cordero-Grande L, Price AN, Hughes E, et al. A framework for multi-component analysis of diffusion MRI data over the neonatal period. *Neuroimage*. 2019 Feb 1;186:321–37.
31. Christiaens D, Slator PJ, Cordero-Grande L, Price AN, Deprez M, Alexander DC, et al. In Utero Diffusion MRI: Challenges, Advances, and Applications. *Top Magn Reson Imaging TMRI*. 2019 Oct;28(5):255–64.
32. Payette K, de Dumast P, Kebiri H, Ezhov I, Paetzold JC, Shit S, et al. An automatic multi-tissue human fetal brain segmentation benchmark using the Fetal Tissue Annotation Dataset. *Sci Data*. 2021 Jul 6;8:167.
33. Fidon L, Viola E, Mufti N, David AL, Melbourne A, Demaerel P, et al. A spatio-temporal atlas of the developing fetal brain with spina bifida aperta. *Open Res Eur*. 2022 Aug 31;1:123.
34. Uus AU, Kyriakopoulou V, Makropoulos A, Fukami-Gartner A, Cromb D, Davidson A, et al. BOUNTI: Brain vOlumetry and aUtomated parcellatioN for 3D feTal MRI [Internet]. *bioRxiv*; 2023 [cited 2024 Apr 25]. p. 2023.04.18.537347. Available from: <https://www.biorxiv.org/content/10.1101/2023.04.18.537347v2>
35. Calixto C, Machado-Rivas F, Cortes-Albornoz MC, Karimi D, Velasco-Annis C, Afacan O, et al. Characterizing microstructural development in the fetal brain using diffusion MRI from 23 to 36 weeks of gestation. *Cereb Cortex*. 2024 Jan 1;34(1):bhad409.

36. Wilson S, Christiaens D, Yun H, Uus A, Cordero-Grande L, Karolis V, et al. Dynamic changes in subplate and cortical plate microstructure precede the onset of cortical folding in vivo [Internet]. *bioRxiv*; 2023 [cited 2024 Apr 23]. p. 2023.10.16.562524. Available from: <https://www.biorxiv.org/content/10.1101/2023.10.16.562524v1>
37. Pattern Recognition and Machine Learning [Internet]. [cited 2024 Apr 24]. Available from: <https://link.springer.com/book/10.1007/978-0-387-45528-0>
38. Chicco D, Warrens MJ, Jurman G. The coefficient of determination R-squared is more informative than SMAPE, MAE, MAPE, MSE and RMSE in regression analysis evaluation. *PeerJ Comput Sci*. 2021 Jul 5;7:e623.
39. Norori N, Hu Q, Aellen FM, Faraci FD, Tzovara A. Addressing bias in big data and AI for health care: A call for open science. *Patterns*. 2021 Oct 8;2(10):100347.
40. Tripathi S, Gabriel K, Dheer S, Parajuli A, Augustin AI, Elahi A, et al. Understanding Biases and Disparities in Radiology AI Datasets: A Review. *J Am Coll Radiol*. 2023 Sep 1;20(9):836–41.
41. Lu YC, Kapse K, Andersen N, Quistorff J, Lopez C, Fry A, et al. Association Between Socioeconomic Status and In Utero Fetal Brain Development. *JAMA Netw Open*. 2021 Mar 1;4(3):e213526.
42. Bastiani M, Andersson JLR, Cordero-Grande L, Murgasova M, Hutter J, Price AN, et al. Automated processing pipeline for neonatal diffusion MRI in the developing Human Connectome Project. *Neuroimage*. 2019 Jan 15;185:750–63.
43. Christiaens D, Cordero-Grande L, Pietsch M, Hutter J, Price AN, Hughes EJ, et al. Scattered slice SHARD reconstruction for motion correction in multi-shell diffusion MRI. *NeuroImage*. 2021 Jan 15;225:117437.
44. BioMedIA/MIRTK [Internet]. Biomedical Image Analysis Group; 2024 [cited 2024 Apr 16]. Available from: <https://github.com/BioMedIA/MIRTK>
45. NumPy - [Internet]. [cited 2024 Apr 21]. Available from: <https://numpy.org/>
46. scikit-learn: machine learning in Python — scikit-learn 1.4.2 documentation [Internet]. [cited 2024 Apr 21]. Available from: <https://scikit-learn.org/stable/>
47. Josef Perktold, Skipper Seabold, Kevin Sheppard, ChadFulton, Kerby Shedden, jbrockmendel, et al. statsmodels/statsmodels: Release 0.14.2 [Internet]. [object Object]; 2024 [cited 2024 Apr 22]. Available from: <https://zenodo.org/doi/10.5281/zenodo.593847>
48. SciPy - [Internet]. [cited 2024 Apr 21]. Available from: <https://scipy.org/>
49. McKinstry RC, Mathur A, Miller JH, Ozcan A, Snyder AZ, Schefft GL, et al. Radial organization of developing preterm human cerebral cortex revealed by non-invasive water diffusion anisotropy MRI. *Cereb Cortex N Y N 1991*. 2002 Dec;12(12):1237–43.

50. Batalle D, O'Muircheartaigh J, Makropoulos A, Kelly CJ, Dimitrova R, Hughes EJ, et al. Different patterns of cortical maturation before and after 38 weeks gestational age demonstrated by diffusion MRI in vivo. *NeuroImage*. 2019 Jan 15;185:764–75.
51. Kostović I, Judas M. The development of the subplate and thalamocortical connections in the human foetal brain. *Acta Paediatr Oslo Nor* 1992. 2010 Aug;99(8):1119–27.
52. Kostović I, Jovanov-Milošević N, Radoš M, Sedmak G, Benjak V, Kostović-Srzić M, et al. Perinatal and early postnatal reorganization of the subplate and related cellular compartments in the human cerebral wall as revealed by histological and MRI approaches. *Brain Struct Funct*. 2014 Jan 1;219(1):231–53.

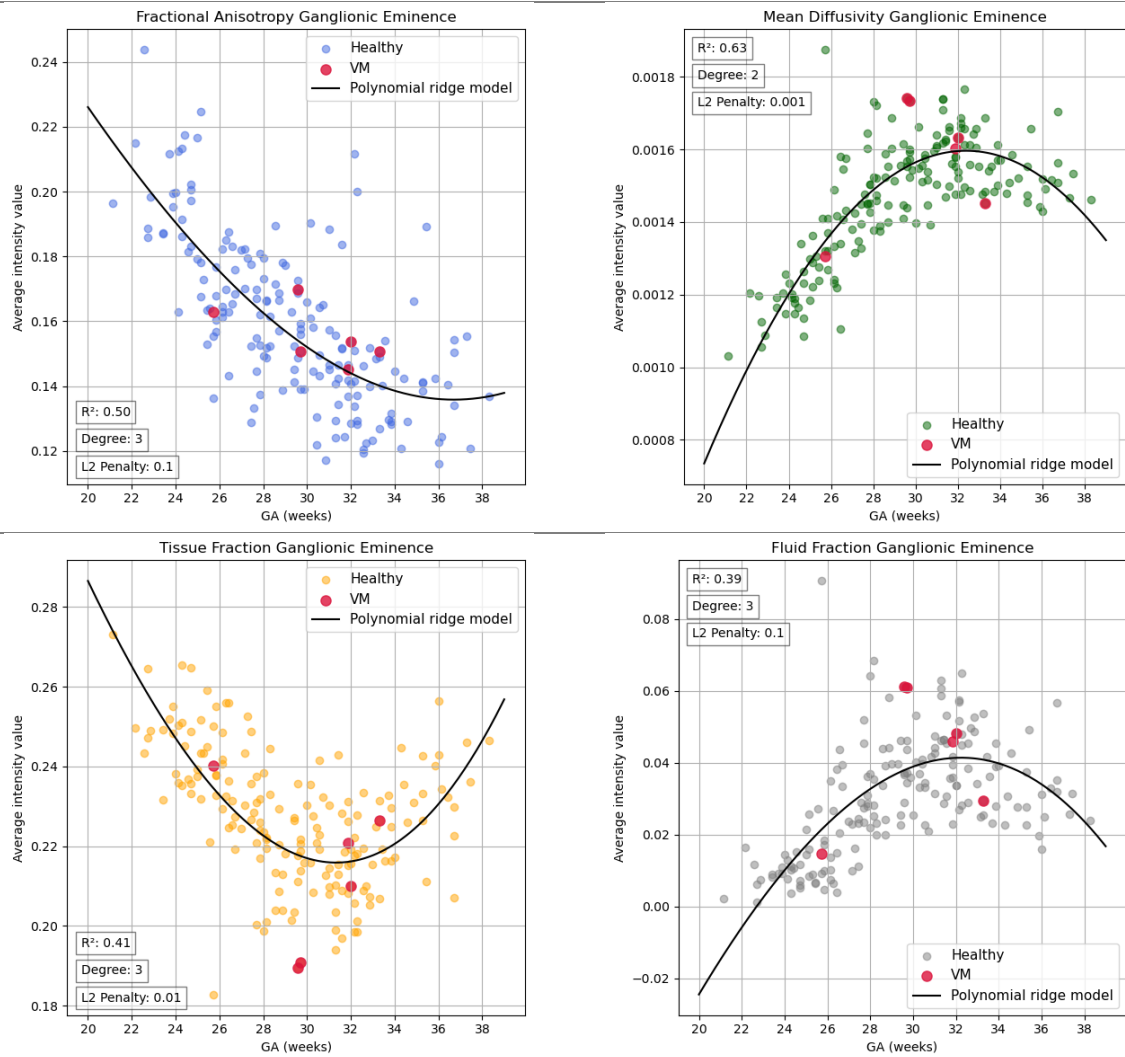
8 APPENDIX

Periventricular white matter

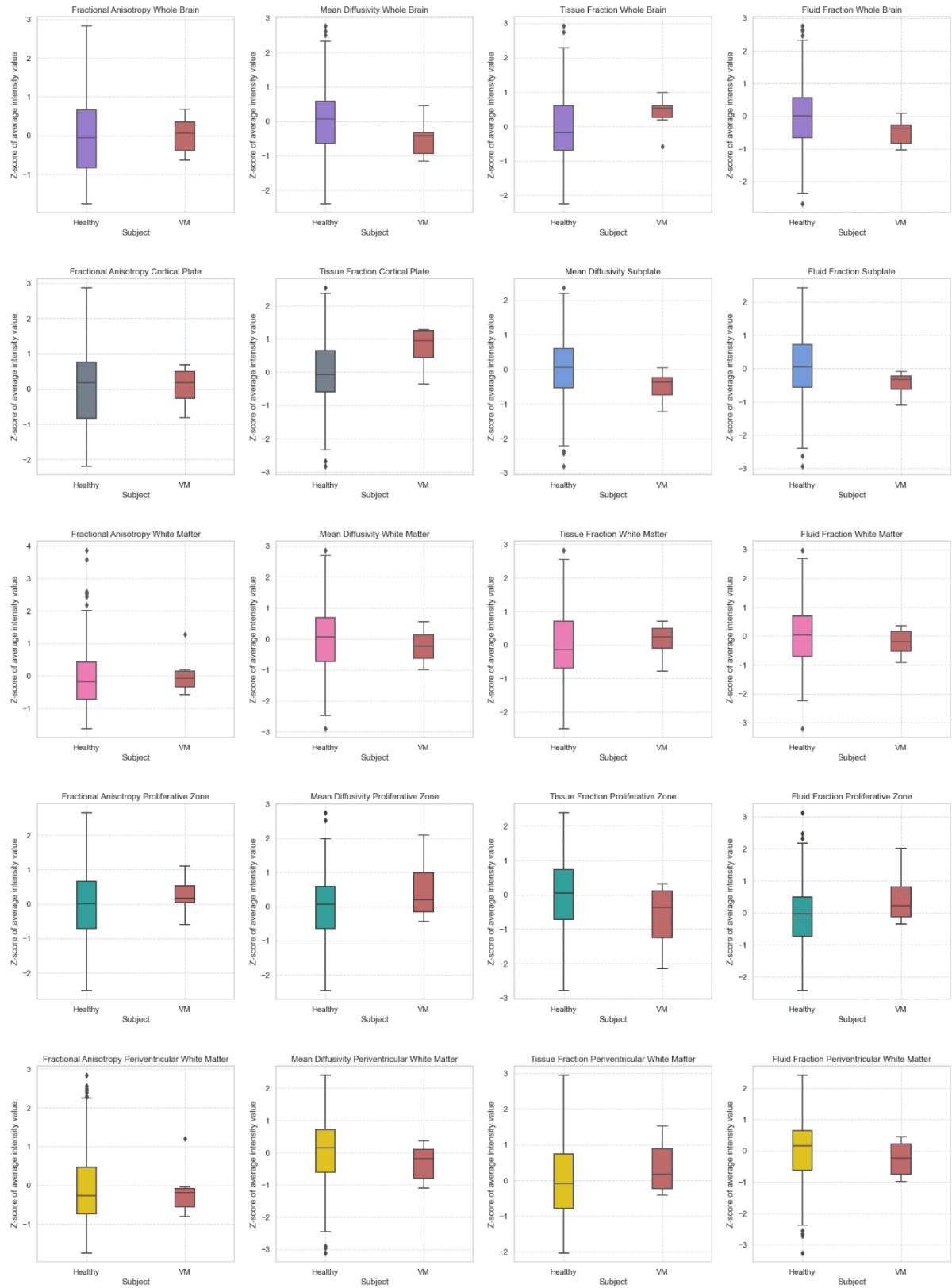


Supplementary Figure 1: Four polynomial ridge models of FA, MD, TF, and FF of PVWM vs GA along with the polynomial degree and L2 penalty selected by cross validation. VM subjects are highlighted in red.

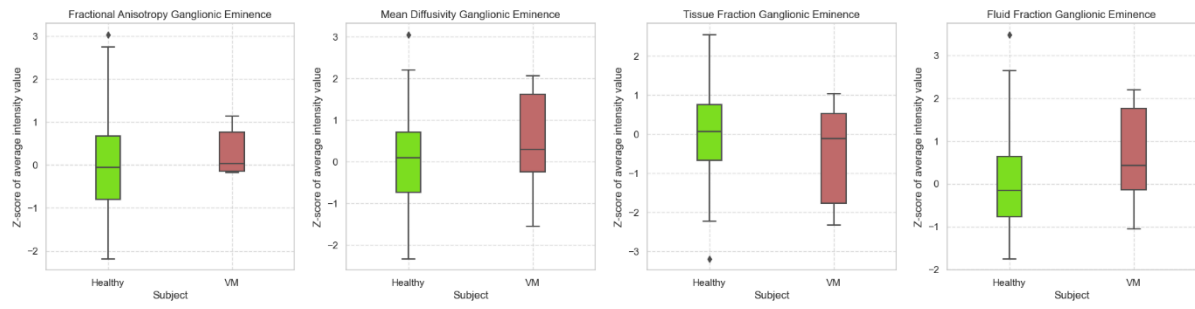
Ganglionic eminence



Supplementary Figure 2: Four polynomial ridge models of FA, MD, TF, and FF of GE vs GA along with the polynomial degree and L2 penalty selected by cross validation. VM subjects are highlighted in red.



Supplementary Figure 3: Box plots comparing z-scores of VM and healthy subjects of the same GA.



Supplementary Figure 4: Box plots comparing z-scores of VM and healthy subjects of the same GA.